Astronomy & Astrophysics

Unintended electromagnetic radiation from Starlink satellites detected with LOFAR between 110 and 188 MHz

F. Di Vruno[1,2,*], B. Winkel[3,2,*], C. G. Bassa[4,*], G. I. G. Józsa[3,2,5,*], M. A. Brentjens[4], A. Jessner[3], and S. Garrington[6,*]

[1] Square Kilometre Array Observatory, Lower Withington, Macclesfield, Cheshire, SK11 9FT, UK
  e-mail: federico.divruno@skao.int
[2] European Science Foundation, Committee on Radio Astronomy Frequencies, 1 quai Lezay Marnésia, BP 90015,
  67080 Strasbourg Cedex, France
[3] Max-Planck-Institut für Radioastronomie, Auf dem Hügel 69, 53121 Bonn, Germany
[4] ASTRON, Netherlands Institute for Radio Astronomy, Oude Hoogeveensedijk 4, 7991 PD Dwingeloo, The Netherlands
[5] Department of Physics and Electronics, Rhodes University, PO Box 94, Makhanda, 6140, South Africa
[6] Jodrell Bank Centre for Astrophysics, Department of Physics and Astronomy, University of Manchester, Manchester M13 9PL, UK

ABSTRACT

We report on observations of 68 satellites belonging to the SpaceX Starlink constellation with the LOFAR radio telescope. Radiation associated with Starlink satellites was detected at observing frequencies between 110 and 188 MHz, which is well below the 10.7–12.7 GHz radio frequencies used for the downlink communication signals. A combination of broad-band features, covering the entire observed bandwidth, as well as narrow-band (bandwidth < 12.2 kHz) emission at frequencies of 125, 135, 143.05, 150, and 175 MHz, was observed. The presence and properties of both the narrow- and broad-band features vary between satellites at different orbital altitudes, indicating possible differences between the operational state of, or the hardware used in, these satellites. While the narrow-band detections at 143.05 MHz can be attributed to reflections of radar signals from the French GRAVES Space Surveillance Radar, the signal properties of the broad- and narrow-band features at the other frequencies suggest that this radiation is intrinsic to the Starlink satellites and it is seen for 47 out of the 68 Starlink satellites that were observed. We observed spectral power flux densities vary from 0.1 to 10 Jy for broad-band radiation, to 10 to 500 Jy for some of the narrow-band radiation, equivalent to electric field strengths of up to 49 dB $\left[\mu\text{V m}^{-1}\right]$ (as measured at a 10 m distance from the satellites, with a measurement bandwidth of 120 kHz). In addition, we present equivalent power flux density simulations of the full Starlink phase 1 constellation, as well as other satellite constellations, for one frequency band allocated to radio astronomy by the International Telecommunication Union (ITU). With these, we calculate the maximum radiation level that each satellite constellation would need to have to comply with regulatory limits for intended emissions in that band. However, these limits do not apply if the radiation is unintended, that is to say if it does not originate from intentionally radiated signals for radio communication or other purposes. We discuss the results in light of the (absence of) regulations covering these types of unintended electromagnetic radiation and the possible consequences for astronomical radio observations.

Key words. light pollution – space vehicles – telescopes – surveys

1. Introduction

Modern radio astronomy has profited greatly from advances in technology. Astronomical radio receivers nowadays are often operated with large fractional bandwidths (bandwidth $\Delta\nu$ over observing frequency ν in excess of $\Delta\nu/\nu > 50\%$; e.g. Torne 2017; Hobbs et al. 2020), increased sensitivity, and aperture (e.g. Jonas & MeerKAT Team 2016), as well as wider fields of view (e.g. Johnston et al. 2007; van Haarlem et al. 2013). At the same time, the numerical capabilities of digital back ends have enormously increased owing to field programmable gate arrays (FPGAs) or graphics processing units (GPUs) that allow one to implement special-purpose algorithms in flexible hardware boosting the processing speeds. This allows one to record data with unprecedented temporal and spectral resolution,
which benefits spectroscopy, pulsar, and very large baseline interferometry (VLBI) observations alike.

However, astronomy is not alone in utilising the radio spectrum. There is a huge number of applications, such as radio and TV broadcasts, high-speed wireless communications (e.g. cell phone networks and WiFi), or radars, which require access to the spectrum. Any type of radio communication and intended radio transmissions is regulated to avoid a situation where different operators – when using the same or nearby frequencies – create interference on each other's systems. This regulation of the radio spectrum is handled at the national level by national radio administrations; however, as radio waves do not care for national borders, international rules are required for harmonisation. The Radiocommunication sector of the International Telecommunication Union (ITU-R) is the top level organisation that takes care of this international regulation. It is a specialised agency of the United Nations. The ITU-R (2020) publishes the Radio Regulations (RR), which is an international treaty and member states are expected to transform the RR into national law.

---

[*] Member of the IAU Centre for the Protection of the Dark and Quiet Sky from Satellite Constellation Interference (IAU CPS).

The ITU-R recognised radio astronomy as a service – the radio astronomy service (RAS) – already in 1959 and allocated bands in the radio spectrum to it. Unfortunately, the bands that are allocated to the RAS are relatively sparse and narrow – for spectral-line observations, the majority of the reserved bands only cover the typical Milky Way Doppler shifts. Also, the total amount of spectrum that is allocated to the RAS is not considered to be sufficient for modern radio astronomical research by most scientists. Below 4 GHz, only 5% of the radio spectrum is allocated to radio astronomy at various levels of protection. If only primary allocations (the highest level of protection) are considered, as little as 1.6% is allocated to the RAS. For more details about the regulatory process, the radio astronomy service and its protection, we refer readers to the ITU Handbook on Radio Astronomy (ITU-R Working Party 7D 2013), the CRAF Handbook for Radio Astronomy (Committee on Radio Astronomy Frequencies 2005), and the Handbook of Frequency Allocations and Spectrum Protection for Scientific Uses (National Academies of Sciences, Engineering, and Medicine 2015).

Not all radiation produced from electronic devices is subject to ITU-R regulations. To a large extent, the RR only cover the so-called emissions, which refer to the radiation that is directly related to the intentional use of radio frequencies in a system (for the purpose of communications, remote sensing, radionavigation, etc.). This obviously includes the wanted signals, but also unwanted emission: spectral sidelobes including harmonics and intermodulation products that are an inevitable by-product of the generation of the wanted transmission. Unwanted emission is a consequence of the signal amplification or mixing, the chosen modulation scheme, etc. Both the wanted and unwanted emissions are regulated in the RR. But there is yet another source of electromagnetic radiation present in any electrical device (or system), which is related at its most fundamental level to the acceleration and deceleration of charges in any electrical or electronic circuits and not necessarily related to the generation of wanted radio signals. As the RR did not coin a regulatory term for this, hereafter we refer to this as unintended electromagnetic radiation (UEMR); it is worth mentioning that in engineering this radiation can be referred to as electromagnetic interference (EMI). UEMR can appear, for example, as the product of current loops in switching mode power supplies, communication signals in unbalanced or mismatched transmission lines, fast switching signals in printed circuits, and actuating electromechanical circuits, etc. Basically any electrical circuit generates some level of UEMR.

UEMR is not explicitly regulated at the ITU-R level, though other standardisation organisations have filled the gap. The Comité International Spécial des Perturbations Radioélectriques (CISPR[1]), which is a part of the International Electrotechnical Commission (IEC), sets standards for all kinds of terrestrial electrical and electronic devices in order to control electromagnetic interference. Unlike the RR, CISPR standards refer not only to radiocommunication systems but all kinds of electronic devices. Furthermore, the standards also cover measurement procedures, which are used to determine the level of UEMR produced by a device under test.

Unlike intended radio emission, UEMR is not clearly specified by a centre frequency, output power and bandwidth, yet it has some characteristics worth mentioning: (i) its radiated power is normally several orders of magnitude lower than any intentional radiation; (ii) UEMR is usually not radiated through an antenna, but mostly through cables and/or the mechanical

structure of the system; therefore, its spatial radiation pattern is usually unknown but likely to be closer to isotropic than that of a directional antenna system; and (iii) UEMR may have spectral contents which can be very variable depending on the type of electrical signals and design of the system.

Telescopes used for radio astronomy normally receive UEMR from terrestrial sources located nearby (distances of kilometres) and predominantly though their sidelobes. There are many examples of radio telescopes dealing with terrestrial UEMR, as is the case of wind farms affecting LOFAR observations[2] or emission from microwaves resembling astrophysical signals (Petroff et al. 2015). Radio astronomers also put great effort into shielding the necessary observation equipment (computers, receivers etc.) to avoid self-made UEMR to enter the data (Swart et al. 2022). Environmental interference (intended and unintended) to radio telescopes can be minimised by building them in designated radio quiet zones or RQZs (Rep. ITU-R RA.2259-1). Unfortunately, RQZs provide no mitigation against radio emission from Earth orbiting satellites, which radio telescopes can receive through their primary beam or near sidelobes. In the case of the Iridium satellite constellation, unwanted radio emissions (i.e. not UEMR) interfered with astronomical observations of the 1612 MHz OH spectral line for more than 20 years (e.g. Cohen 2004; ECC Report 171; ECC Report 247). Studying reflections of terrestrial signals from satellites, Prabu et al. (2020) reported possible UEMR of two cubesats using the MWA between 80 and 103 MHz.

The proliferation of the new and large satellite constellations in low Earth orbit (LEO) – often referred to as megaconstellations – has caused worries in the astronomical community owing to the satellites ability to reflect sunlight and to emit radio signals (e.g. McDowell 2020; Hainaut & Williams 2020; Boley & Byers 2021). This led to the Satellite Constellations workshops (SATCON1 and SATCON2; Walker et al. 2020b), the Dark & Quiet Skies I and II workshops (Walker et al. 2020a, 2021) and the founding of the IAU Centre for the Protection of the Dark and Quiet Skies from Satellite Constellation Interference (IAU CPS), the members of which investigated and continue to investigate the possible impact of large LEO satellite constellations on astronomy (see Rawls et al. 2020; Bassa et al. 2022; Di Vruno & Tornatore 2023). Owing to the increasing total number of satellites in LEO, and hence the increasing probability that a satellite appears within the field of view of a radio telescope, it makes sense to consider satellite UEMR as a potential source of interference in the future. The potential threat posed by satellite UEMR from large constellations was first considered at the Dark & Quiet Skies II workshop (Walker et al. 2021).

In this paper, we investigate the potential impact of satellite UEMR on radio astronomy through observations of the SpaceX Starlink satellite constellation. At the time of the observations presented here, this constellation was the largest in orbit with some 2100 satellites in orbit. This constellation provides broad-band internet connectivity with radio emission used for downlinks allocated to the 10.7–12.7 GHz frequency band[3]. Compatibility with radio astronomy observations in the protected 10.6–10.7 GHz band has previously been studied by the Electronic Communications Committee (ECC) of the European Conference of Postal and Telecommunications Agencies (CEPT)

---

[1] English: International Special Committee on Radio Interference.

[2] https://www.astron.nl/test-wind-turbine-near-lofar-meets-agreed-radio-emission-norms-2/

[3] https://fcc.report/IBFS/SAT-MOD-20200417-00037/2274316

in its ECC Report 271. As UEMR is predominantly expected at low frequencies (below ~1 GHz) (see Pulkkinen 2019), well below the allocated radio transmission downlinks, we observed satellites belonging to the Starlink constellation at frequencies between 110 and 188 MHz with the LOFAR radio telescope (van Haarlem et al. 2013).

This paper is organised as follows; Sect. 2 presents an overview of standards and regulations applicable to satellites and their subsystems, while Sect. 3 uses simulations to investigate the potential aggregate impact of several satellite constellations and its maximum radiated power to comply with the ITU-R threshold levels in one of the protected radio astronomy bands. We describe the observations and their processing in Sect. 4 and discuss the analysis of the detected signals in Sect. 5. Finally, Sect. 6 contains a summary and conclusions.

2. UEMR of satellite systems

Typical satellites are composed of many different modules called subsystems, each one fulfilling a specific function for the satellite to operate. Satellite manufacturers make use of electromagnetic compatibility (EMC) to ensure that all the different subsystems will be compatible with each other. A typical EMC programme focuses on testing each subsystem to ensure that sufficient margins exist between emissions and susceptibilities for the ensemble to work without self-interference.

There are some EMC standards dedicated to space missions, such as the NASA MFSC-SPEC-521 or the ESA ECSS-E-ST-20-7C, most of them based on the US military standard MIL-STD-461. These EMC standards define, among other things, the maximum level of electromagnetic radiation that equipment can generate. Most standards for space are more stringent than the ones used for commercial apparatus such as CISPR-32 (see Fig. 1) but that is not a hard requirement, as a satellite does not need to be compatible with ordinary commercial equipment.

Once completely assembled, a satellite is usually characterised by a 'system level' test that evaluates the overall UEMR (among many other parameters) of it as a whole. These tests can last for weeks, depending on the complexity of the satellite, making it a very expensive activity. For this reason, system level tests tend to focus on the minimum and necessary checks for each parameter of a complete satellite. A clear example of this can be seen in Blondeaux et al. (2016), where UEMR is not highlighted as an important step to characterise a satellite constellation.

While commercial standards such as the IEC 61000 family, CISPR or the US Federal Communications Commission (FCC) part 15 (see Fig. 1), are harmonised and mandatory to allow entry into a certain market, there is currently no international agency or space law that requires a spacecraft to comply to a certain EMC standard. Furthermore, the information about which EMC standard is used for a specific programme, the considered UEMR thresholds, or the real level of emissions are rarely made public. Few examples are in the public domain such as Yavaş & Akgül (2019) and Elkman et al. (2007). Informal communications with satellite industry specialists indicated that the normal practice for satellite level UEMR tests is to set an emission threshold relatively high (which speeds-up testing times) and only apply stringent levels (long testing times) to narrow frequency bands where the satellite or the rocket-launcher have receivers or sensitive instruments. In Yavaş & Akgül (2019), results of a satellite emission level test are shown, where the limit threshold (marked as a solid red line in their Fig. 7) is defined at very high levels of emission almost for every frequency with the exception of a few communication bands.
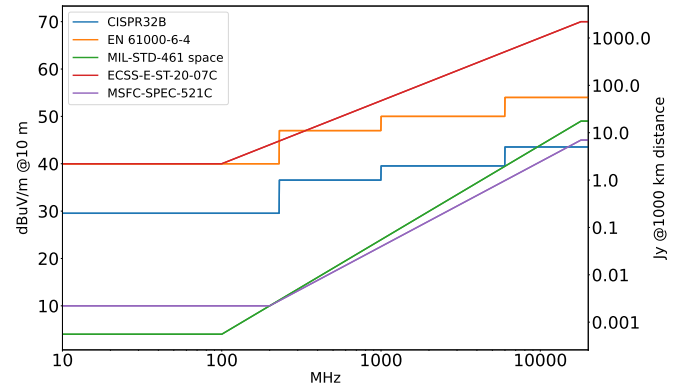

Fig. 1. Radiated emission limits for several EMC standards such as commercial (CISPR, EN61000), military (MIL-STD-461), and space (MSFC and ECSS). Left axis shows electric field measured at 10 m distance, right axis shows equivalent spectral power flux density (in Jy) assuming a source at 1000 km distance.

Owing to this lack of information, we can suppose that a satellite could emit relatively strong UEMR signals, outside of the bands of interest for the manufacturer or operator, and still pass this type of testing. This is not an unlikely situation, since many subsystems can aggregate their emissions or their interconnection can change the electromagnetic configuration of the satellite and increase the emissions in a certain frequency band. This may not have been an issue in the past, with very small constellations or with single satellite systems. Even if a satellite had strong UEMR, it would require a very sensitive receiver to detect it or in other words would require the satellite to be in the main lobe of a radio telescope for a considerable fraction of an observation: a very rare condition until recently.

With the advent of the large LEO satellite constellations (such as Starlink phase 1 with 4408 satellites or OneWeb phase 1 with 720 satellites[4]) the situation changes. Firstly, the number of LEO satellites leads to an increase of the aggregate signal, which might become large enough to cause interference even through the sidelobes and increases the probability of a detection in the main lobes of the radio telescope. Secondly, the new satellites are manufactured in series, therefore it is possible that many satellites present similar UEMR. These two effects could make the situation for radio astronomy complicated, even in radio bands reserved to radio astronomy.

3. Potential impact of satellite EMR on RAS

To investigate the potential impact of satellite EMR on radio astronomical observations, it is possible to make use of the established methods that were developed by ITU-R for regular compatibility calculations of wanted and unwanted emissions. The ITU-R recommends to use the equivalent power flux density (EPFD) method (see Rec. ITU-R S.1586-1; Rec. ITU-R M.1583-1). A satellite constellation is simulated over a given time range. The power received from each satellite can be calculated from the transmitted power, taking into account transmitter and receiver antenna gains and path propagation losses (e.g. line of sight losses, atmospheric attenuation) before it enters the radio astronomy receiver. The total aggregated power, which is the sum of all power contributions, can be then determined. Under the assumption of standardised characteristics of the receiving antenna, the received power can also be

---

[4] https://planet4589.org/space/con/conlist.html

converted to the associated power flux density (PFD, known as total or integrated flux density in the radio astronomy community), which allows to conveniently compare it to PFD threshold levels that are defined in regulations for the protection of a victim station. An advantage of this conversion is that it makes a better comparison possible between different receiving stations, which usually have different antenna patterns and gains. For example, the RAS protection criteria (Rec. ITU-R RA.769-2; in Tables 1 and 2) are provided for an isotropic receiver, although in reality radio telescopes usually have very high forward gain.

3.1. Assessing the aggregate impact of a satellite constellation

In the following, the EPFD method is used to determine the potential impact of UEMR from different satellite constellations on radio astronomy observations. The EPFD method is widely used in spectrum management and is well documented in ITU-R documents. For convenience, a more detailed summary is provided in Appendix A. Here, the basic steps are explained in a simplified form. To calculate the received power for one particular pointing direction of the receiver antenna and a certain satellite orbit configuration, the procedure is as follows.

In the first step the satellite positions (and transmitter antenna orientations) with respect to the observer are be determined for a number of time steps and for a given period of time. The required time resolution mostly depends on the satellite altitudes. For low-earth orbit (LEO) satellites the time resolution should be 1 s or less as the angular velocities are high. Then the link budget (path propagation losses as well as transmitter and receiver antenna gains) between satellites and observer are computed. As the satellites are not necessarily in the main beam of the radio telescope, the angular separation between the antenna pointing direction and the geometrical position of the satellites needs to be accounted for, which changes the effective receiver gain. Likewise, the observer will usually not be situated in the forward direction of the satellite antenna. Modern satellites are often equipped with active antennas that allow electronic beam-forming in real-time, such that the effectively transmitted power towards the observer can fluctuate strongly. It should be noted, however, that in the case of UEMR, given its nature, a high directivity is not expected to be reached and an isotropic transmitting antenna pattern is used hereafter as an approximation. After the link budget is calculated, all the individually received powers (from each satellite) are added, which yields the total aggregated power. Finally the total aggregated power received at the radio telescope is compared to the permitted threshold levels, for example defined in Rec. ITU-R RA.769-2. In this recommendation, the RAS protection levels are specified for an integration time of 2000 s, thus it is necessary to simulate the orbits over this time span.

The calculation is performed for a grid of sky cells (or telescope pointing directions) having approximately equal solid angles. This allows to analyse the spatial distribution of the contributed power levels. To assess statistical scatter, the whole simulation is repeated hundreds or thousands of times for different starting times and antenna pointings within the grid cells.

Often, the power flux density at the observer location (caused by the satellites) is transformed into the so-called equivalent power flux density (EPFD). This is the power flux density, which would need to be present in the boresight of a radio telescope to create the same power as the aggregated power from all satellites. Appendix A contains more details on this.

3.2. EPFD and large satellite constellations

For some of the large satellite constellations under construction, in particular SpaceX/Starlink and OneWeb, EPFD calculations were performed by the Electronic Communications Committee (ECC) of the European Conference of Postal and Telecommunications Administrations (CEPT) in its ECC Report 271. In that report, the out-of-band emissions of the satellite downlinks in the RAS band at 10.60–10.70 GHz were analysed by means of this method.

To our knowledge, UEMR from large satellite constellations in operation has never been studied nor measured, probably because the number of satellites (of the same design) was not large enough to even be considered a problem, but this situation has changed now. Using the EPFD method it is possible to determine the maximum UEMR that each single satellite of a constellation may radiate in the 150.05–153 MHz primary radio astronomy band, while not producing harmful interference. Here we consider harmful interference as defined in Rec. ITU-R RA.769-2.

The 150.05–153 MHz frequency band, which is allocated to the RAS, was chosen as it is commonly accepted that radiation caused by electronic circuits is mainly concentrated below 1 GHz, and it falls within the observing band of LOFAR. The harmful interference threshold in this band is $-194\,\mathrm{dB}\left[\mathrm{W\,m^{-2}}\right]$ over a bandwidth of about 3 MHz, according to Rec. ITU-R RA.769-2 (see their Table 1).

Given that the actually radiated emissions from a single satellite are unknown, we have to assume some value. An electric field strength of $30\,\mathrm{dB}\left[\mu\mathrm{V\,m^{-1}}\right]$ is a typical radiation level[5] found in commercial standards such as CISPR-32 based on a detector bandwidth of 120 kHz and measured at a distance of 10 m. This number is equivalent to a radiated spectral power of $-45.6\,\mathrm{dB}\left[\mathrm{mW\,MHz^{-1}}\right]$. We also assume in our simulations that this radiation is constant in time and frequency within the studied band. In practice this is certainly not the case. UEMR features can be time-variable and could also be narrow-band and in such a case a bandwidth correction factor would need to be applied. We furthermore work under the simplification that satellite UEMR is isotropically radiated.

The RAS antenna pattern and gain used in the calculations depends on the type of radio telescope. At these low frequencies, mostly interferometric telescopes are used, such as LOFAR and SKA1-Low. The actual antenna patterns of interferometers (after beam-forming and correlation) are complex and are not perfectly described by the Rec. ITU-R RA.1631-0 model. Therefore, we perform the EPFD assuming parabolic-dish antennas of diameter 25-m and 70-m, respectively, which approximately have the same effective antenna area as SKA1-Low tiles and LOFAR (international) stations. In our simulations it is assumed that the RAS station is located at the geographical latitude of LOFAR, 53° N.

---

[5] The value of $30\,\mathrm{dB}\left[\mu\mathrm{V\,m^{-1}}\right]$ in CISPR refers to a so-called quasi-peak detector. Here, we assume that field strength to be the average over the measurement period. Usually, the two detector types may lead to significantly different outputs – by several dB – depending on the properties of the signal (compare Winkel & Jessner 2019, and references therein).

Table 1. Results of the EPFD simulations.

Satellite System	# Sats	Avg. alt. (km)	Max. E-field (dB[μV m^{-1}])	
			$d = 25$ m	$d = 70$ m
Spire	118	500	$26.1^{+2.3}_{-0.9}$	$23.4^{+2.0}_{-0.7}$
Iridium NEXT	66	780	$30.1^{+0.4}_{-0.2}$	$26.7^{+0.5}_{-0.6}$
OneWeb	720	1200	$23.1^{+0.2}_{-0.1}$	$21.6^{+0.2}_{-0.2}$
SpaceX/Starlink	4408	560	$11.7^{+0.1}_{-0.1}$	$9.9^{+0.1}_{-0.1}$
SpaceX/Swarm	150	500	$26.2^{+1.4}_{-1.1}$	$23.6^{+1.9}_{-0.9}$

Notes. To avoid exceeding the RAS threshold levels in the band 150.05–153 MHz, the electric field values produced by satellites (measured with a 120 kHz detector at 10 m distance) should be lower than the stated E-fields. This assumes that the UEMR has broad-band type, or more precisely that the signal is constant over the full RAS band, 150.05–153 MHz. With a measurement bandwidth of 2.95 MHz the electric field limits are (2950/120) = 13.9 dB higher.

Using these parameters and assumptions, EPFD calculations were carried out for a number of existing or currently in-deployment satellite constellations: Spire[6], Iridium NEXT[7], OneWeb[8], SpaceX/Starlink[9], and SpaceX/Swarm[10]. This provides us a range of constellation sizes from 66 satellites up to 4408 (see Table 1) in various orbital configurations. For the satellite position calculations we made use of the open-source Python package `cysgp4`[11] (Winkel 2023), which is available under GPL-v3 license. It is a wrapper around the `sgp4lib`[12] C++ implementation of the simplified perturbation model SGP4 (see also Vallado et al. 2006). Furthermore, the `pycraf`[13] Python package (Winkel & Jessner 2018a,b) was used, which provides implementations for a number of relevant ITU-R Recommendations. It is also available under GPL-v3 license.

3.3. Simulation results

For each constellation in Table 1, one hundred iterations (simulation runs) were processed, which allows us to assess the statistical scatter of the results. As an example for the results, Fig. 2 shows the cumulative distribution function for EPFD values for the Iridium NEXT and Starlink constellations with the assumption of UMR with an electric field strength of 30 dB $\left[\mu\text{V m}^{-1}\right]$ over the full RAS bandwidth[14] and a RAS antenna with a 70-m diameter located a geographic latitude of 53° N. The light green and blue curves in the figure show the results for all sky cells in each individual simulation run, while the darker curves represent
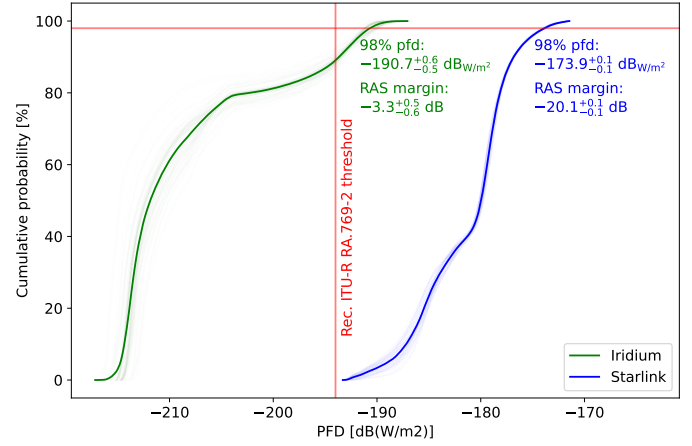
---

[6] https://fcc.report/IBFS/SAT-LOA-20151123-00078/1126653
[7] https://fcc.report/IBFS/SAT-AMD-20151022-00074/1145619
[8] https://fcc.report/IBFS/SAT-LOI-20160428-00041/1135071
[9] https://fcc.report/IBFS/SAT-MOD-20200417-00037/2274316
[10] https://fcc.report/IBFS/SAT-LOA-20181221-00094/1592875
[11] https://pypi.org/project/cysgp4/
[12] https://github.com/dnwrnr/sgp4
[13] https://pypi.org/project/pycraf/
[14] If there was only a narrow-band signal within the RAS band, a correction factor would need to be applied.

Fig. 2. Cumulative distribution functions for EPFD values owing to Iridium NEXT and Starlink, assuming an isotropic transmitter spectral power of -45.6 dB $\left(\text{mW MHz}^{-1}\right)$ and a 70-m radio telescope located a geographic latitude of 53° N.
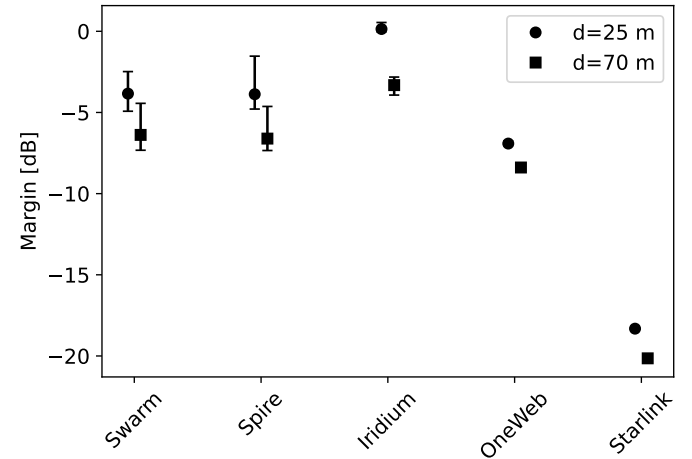

Fig. 3. Calculated margins for all simulated satellite constellations with the assumption of a 30 dB $\left[\mu\text{V m}^{-1}\right]$ UEMR with respect to the ITU-R thresholds in 150.05$-$153 MHz.

the median of the individual runs in each sky cell. Rec. ITU-R RA.1513-2 recommends that the total data loss caused by a single interfering system should not exceed 2%, which is indicated by the horizontal red line (the 98% percentile) in the figure. The vertical red line marks the Rec. ITU-R RA.769-2 threshold. The cumulative probability at which this threshold is exceeded can be used to determine the actual expected data loss (about 10% for Iridium NEXT and 100% for Starlink with the assumptions used in the simulation). The intersection between the cumulative probability curve and the horizontal red line of 98% percentile yields the so-called margin, that is the difference between the RAS threshold and the actual received power flux density. If it is negative, emissions from the respective satellite constellation ought be below the assumed model values by that amount in order to comply with the thresholds in the RAS band. The inferred margins for all satellite constellations are presented in Fig. 3.

Based on the margins, under the assumptions used in the simulation, it is possible to determine a maximum electric field value that each satellite should comply with to ensure that the received power at the RAS station is not in excess of the permitted RAS threshold levels at the data loss of 2%. These values
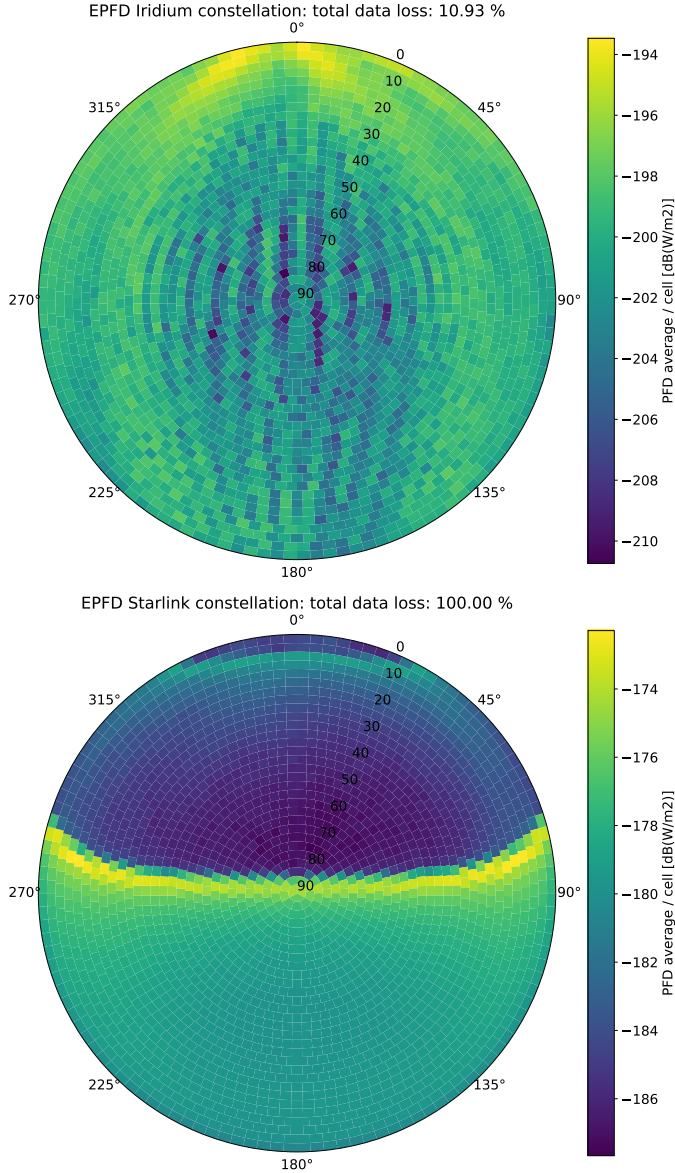
Fig. 4. EPFD received in each sky cell (average over 100 iterations) owing to Iridium NEXT and Starlink constellations in topocentric frame (azimuth and elevation) as received by a 70-m RAS antenna.

Fig. 5. Beam pattern of the LOFAR observation in equatorial coordinates (right ascension and declination). The 91 tied-array beams are indicated with the smaller circles (24′ FWHM at 150 MHz), while the larger dashed circle denotes the FWHM of a LOFAR core station (4°.7 at 150 MHz). Predictions of the motion of Starlink satellites with respect to the beam pattern are indicated with the blue (at orbital altitude $h = 358$ km) and orange (at $h = 550$ km). The small and large black circles indicate the ingress into and egress from the tied-array and station beams, respectively.

section describes the observation method, data calibration and processing, and different types of detected signals.

4.1. Observations

LOFAR, the Low Frequency Array (van Haarlem et al. 2013), is a network of telescopes with stations spread over Europe and a dense core in the north of the Netherlands. We obtained a 1-h observation targeting mostly SpaceX/Starlink satellites on 2022 April 1, starting at 18:30:00 UTC. Radio signals from the High Band Antennas (HBA) of the central six LOFAR core stations, those on the Superterp, were coherently beam-formed by the COBALT beam-former (Broekema et al. 2018) to form 91 tied-array beams (TABs). The TABs were distributed in five hexagonal rings covering the 4°.7 full width at half maximum (FWHM) station beam, each ring separated by 24′ from the next; see Fig. 5. This separation was chosen such that the TABs overlap at the half-power point around 150 MHz, assuming circular beams with a 24′ FWHM at 150 MHz. For each tied-array beam, (uncalibrated) Stokes I intensities in the form of dynamic spectra were recorded between 110 and 188 MHz, with 10.48 ms time resolution and 12.21 kHz frequency resolution.

The TABs were centred towards, and tracking, $\alpha_{J2000} = 08^h00^m00^s$ and $\delta_{J2000} = +49°30'00''$. This pointing direction was chosen for its high Galactic latitude ($b = 31°.1$ at Galactic longitude $l = 169°.4$) and hence low sky temperature (reducing the overall system temperature), as well as the high elevation above the horizon of LOFAR (maximum elevation of 86°.5 at 18:54 UTC), minimising the range between Starlink satellites at their operational altitude of 550 km. Furthermore, at the latitude

are summarised in Table 1. It is noted that the calculated values are lower than commercial EMC standard thresholds such as the CISPR-32 Class B with 30 dB $\left[\mu V\, m^{-1}\right]$.

It is also possible to investigate the regions on the visible (topocentric) sky, which contribute most to the overall received flux density, see Fig. 4, which shows the average EPFD per sky grid cell for the Iridium NEXT and Starlink constellations assuming a 70-m RAS antenna.

4. Observations, data calibration and signal detection

Based on the results obtained in Sect. 3, especially the ones for large satellite constellations such as Starlink, we conducted an observation with the LOFAR telescope which not only covers the frequency range of interest but can also produce multiple beams simultaneously increasing the probability of detecting satellite emissions within a reasonably short campaign. This
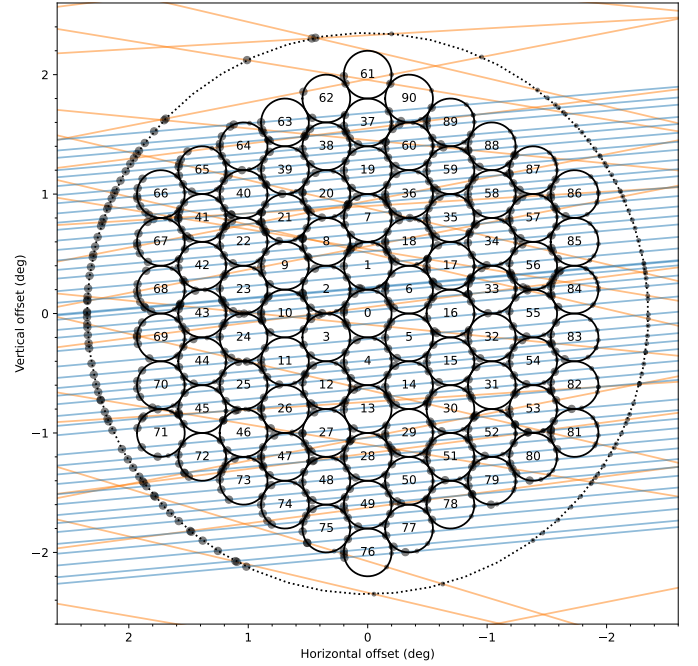
of LOFAR ($\phi = 52°92$), the currently most populated Starlink shells (with orbital inclinations of 53°0 and 53°2) lead to over-densities of satellites per unit area of sky near LOFAR's zenith (Bassa et al. 2022; Lawler et al. 2022), maximising the number of Starlink satellites passing through the TABs.

We used public ephemerides[15] of the Starlink satellites generated by SpaceX for the observation planning and the processing of the data. The public ephemerides provide predictions for position and velocity of each Starlink satellite with respect to an Earth-centred inertial coordinate frame at 1 min time intervals, and include planned manoeuvres to adjust the satellite orbit. From these ephemerides, the trajectory of each satellite passing through the LOFAR beam pattern during the 1 h observation was calculated, resulting in the passes shown in Fig. 5. We also computed the time of ingress and egress of each satellite through the station beam and the TABs. We note that individual Starlink satellites are known to make small unplanned manoeuvres, which generally result in the satellite passing early or late compared to predictions, without significantly altering its trajectory on the sky. The ephemerides show that a total of 68 individual Starlink satellites passed through the LOFAR station beam during the 1 h observation, 22 of which were at the operational altitude of $h = 550$ km. The other 46 Starlink satellites passing through the beam pattern were at an altitude of 350 km. These satellites belonged to a group of 48 satellites launched on 2022 March 9, 23 days before our observations, and were still raising their orbits to operational altitudes. The Starlink satellites of this launch are of a newer version 1.5 type[16] compared to the Starlink satellites at the operational altitudes, which reportedly are version 1.0.

The properties of these satellites and their passes through the beam pattern are provided in Table 2. Owing to the high elevation of the observations above the horizon, the distances to the Starlink satellites in the operational orbits at 550 km was around 555 km, while the orbit raising group were at distances of around 356 km. These distances are in the far field of the LOFAR Superterp, whose maximum baseline of ∼300 m puts the Fraunhofer distance from 66 to 113 km for the observed LOFAR band of 110 to 188 MHz. At these distances, the satellites crossed the 4°7 FWHM of the station beam within 6 and 4 s, respectively, while the 24′ TABs were crossed within 0.54 s for satellites at 550 km altitude, and 0.34 s for those at 350 km altitude (t_{pass} column of Table 2). Of the 68 satellite passes, only two did not pass through any of the TABs, while the majority of the others passed through several adjacent TABs, as indicated by the n_{TAB} column in Table 2. Finally, we note that all Starlink satellites passing through the beam pattern during this observation were illuminated by the Sun, and that their solar panels could have been generating power.

4.2. Data calibration

To calibrate the recorded data-sets, we performed both the frequency-dependent system gain (band-pass) correction[17] as well as the intensity calibration. For a single dish antenna, the on-source, off-source method represents a useful strategy to correct for the system gain. In very simple terms, the recorded uncalibrated power spectrum, $P(t_i, f_j)$, at time, t_i and in frequency

channel f_j is related to the actual antenna temperature, T_A, via the receiver system transfer function, $G_{bp}(t_i, f_j)$. G_{bp} is a function of frequency, but it also depends mildly on t_i owing to slow drifts of the receiver (amplifier) gain. For the accuracy required for this project, one can safely assume that G_{bp} is constant with time over the relatively short observation period. Thus,

$$P(t_i, f_j) = G_{bp}(f_j)T_A(t_i, f_j). \tag{1}$$

The idea of the on-source, off-source method is to divide two spectra to remove the frequency-dependent band-pass shape (compare Winkel et al. 2012). This yields

$$\frac{T_{source}}{T_{sys}} = \frac{P^{on}}{P^{off}} - 1, \tag{2}$$

where it was assumed that $T_A^{on} = T_{source} + T_{sys}$, while $T_A^{off} = T_{sys}$. The quantity T_{source} denotes the signal from a source to be measured, which would only be in the on-source spectrum, while all other constituents to the antenna temperature are denoted as system temperature, T_{sys}. Of course, anthropogenic signals, which are often highly variable with time and frequency, would produce residual imprints in the resulting data and ideally needs to be treated before the method is applied. Furthermore, any astronomical signal that is present in both the on- and off-source observation (e.g. large-scale continuum radiation) would also not be processed properly by the method.

Classically, the on-source, off-source strategy involves position switching as one needs a measurement without the (astronomical) source of interest for the reasons explained above. However, LEO satellites are within the observation beam for a very short amount of time, only. Thus, the off-source spectrum can simply be constructed by choosing data at a different time, for example shortly before and after a satellite crosses the beam, and taking the average spectrum over this time range. Another possibility would be to determine the off-source spectrum over the full time span of the observation, for example by averaging all spectra leaving out those that are associated with satellite crossings. The second method should only be applied, though, if the temporal stability of G_{bp} is sufficient. Here, both strategies have been tried out and no significant difference in the calibrated data-sets was found. In practice, all the averaging steps in the above procedures could also make use of the median estimator, which is more robust against outliers, produced by short-term anthropogenic signals.

Obviously, the beam-formed LOFAR data is not measured with only a single antenna. Nevertheless, the method outlined above can still be used in a very similar manner. The measured power spectrum, P, is again subject to a frequency dependent 'system gain', which is now acting on an 'effective (ensemble) antenna temperature' instead of each element's antenna temperature. The on-source, off-source method will remove the imprint of this system gain from the data, but the resulting quantity is not simply T_{source}/T_{sys} as in Eq. (2) but a different quantity.

For the absolute flux calibration we used the approach outlined in Kondratiev et al. (2016) which models the effective area, beam shape, system temperature and coherence of LOFAR. The radiometer equation (e.g. Dewey et al. 1985) relates the (power) flux density root mean square (RMS) at TAB level to these quantities by

$$\Delta S_\nu^{tab} = \frac{\Delta T^{station}}{\Gamma_{tab}} = \frac{1}{\Gamma_{tab}} \frac{T_{sys}^{station}}{\sqrt{n_p t_{obs} \Delta\nu}}, \tag{3}$$

Table 2. Properties of the Starlink satellite passes through the LOFAR beam pattern.

NORAD/COSPAR	d (km)	t_{mid} (s)	t_{pass} (s)	Δt (s)	n_{TAB}	S_ν (Jy) 116–124 (MHz)	125 (MHz)	135 (MHz)	143 (MHz)	150 (MHz)	150.05–153 (MHz)	157–165 (MHz)	175 (MHz)
47373/2021−005AA	554.7	34.66	6.26	+0.00	11	1.1(1)	73(3)	15(1)		13(2)	0.8(1)	0.4(1)	501(28)
47371/2021−005Y	553.6	365.68	5.04	+0.05	8	1.0(1)	72(3)	14(1)			0.5(1)	0.2(1)	
47597/2021−009BB	553.7	400.77	3.83	−0.01	4	0.9(1)	68(5)	15(2)			0.3(1)		
47645/2021−012AB	553.6	646.62	5.83	+0.15	13	1.0(1)	77(3)	12(1)			0.4(1)	0.1(1)	8(1)
47595/2021−009AZ	553.8	731.25	6.13	+0.14	11	1.1(1)	54(3)	13(1)			0.5(1)	0.1(1)	
47596/2021−009BA	554.5	1061.19	5.56	+0.04	10	1.1(1)	81(4)	7(1)			0.5(1)		85(6)
45705/2020−035BA	554.4	1101.86	5.50	−0.06	10	1.0(1)	82(3)	14(1)			0.5(1)	0.1(1)	24(2)
45661/2020−035E	553.4	1432.54	6.11	−0.02	11	1.2(1)	72(3)	21(1)			0.8(1)	0.3(1)	7(1)
45677/2020−035W	553.1	1763.14	3.76	−0.08	4	1.0(1)	72(5)	12(2)			0.3(2)		132(13)
45235/2020−012BK	553.3	1798.44	4.88	−0.01	7	0.9(1)	16(1)	12(1)	79(5)		0.2(1)		
45186/2020−012J	554.0	2128.86	6.26	+0.09	11	1.2(1)	83(3)	14(1)		7(1)	0.3(1)	0.1(1)	322(18)
47621/2021−012B	555.4	2167.83	1.07		0								
47666/2021−012AY	555.0	2374.54	5.36	+0.11	9	1.0(1)	72(3)	8(1)			0.6(1)	0.1(1)	12(2)
45187/2020−012K	555.6	2459.64	4.40	+0.07	6	0.7(1)	11(2)	6(2)	37(5)				
47625/2021−012F	554.6	2498.09	6.02	+0.65	12	0.8(1)	69(3)	11(1)			0.4(1)		8(1)
47651/2021−012AH	554.4	2744.72	6.15	+0.02	11	1.0(1)	84(4)	10(1)		10(1)	0.6(1)	0.2(1)	506(29)
47620/2021−012A	554.4	2829.89	5.88	−0.05	10	1.0(1)	84(3)	11(1)		6(2)	0.4(1)		30(2)
52003/2022−025AZ	356.1	2857.64	2.98	+0.07	6	3.0(2)			37(4)		0.8(2)	0.9(1)	
47636/2021−012S	553.8	2864.70	1.77		0								
52002/2022−025AY	356.2	2866.81	3.11	−0.03	8	0.9(1)			34(4)		1.2(2)	1.7(2)	
52000/2022−025AW	356.5	2877.57	3.21	−0.09	8	0.6(1)			28(3)		0.4(1)	1.1(1)	
52001/2022−025AX	356.1	2887.59	3.32	−0.12	9	1.7(1)			26(3)		1.2(2)	1.6(1)†	
51998/2022−025AU	356.4	2897.50	3.38	−0.07	10	4.8(2)			30(3)		0.8(1)	1.3(1)†	
51999/2022−025AV	356.6	2908.06	3.47	+0.01	10	0.8(1)			9(2)		2.5(2)	1.6(1)†	
51996/2022−025AS	356.5	2918.15	3.54	−0.06	11	3.0(1)			28(3)		0.7(1)	2.2(1)	
51994/2022−025AQ	356.7	2927.70	3.60	−0.02	11	5.1(2)			30(3)		1.7(2)	1.8(1)†	
51992/2022−025AN	356.7	2937.59	3.67	−0.06	11	0.8(1)			19(2)		1.0(1)	1.6(1)†	
51997/2022−025AT	356.3	2947.11	3.72	−0.11	11	2.8(1)			16(2)		0.7(1)	2.5(2)†	
51995/2022−025AR	356.4	2958.22	3.76	−0.02	11	3.6(1)			35(3)		1.4(1)	1.1(1)†	
51990/2022−025AL	356.4	2968.25	3.81	−0.03	11	5.7(2)			38(4)		1.5(1)	1.9(1)	
51993/2022−025AP	356.8	2979.25	3.84	−0.04	11	3.3(1)			25(3)		1.3(1)	1.2(1)†	
51988/2022−025AJ	356.6	2987.83	3.89	+0.33	11	0.5(1)			4(2)		3.4(2)	6.7(4)†	
51986/2022−025AG	356.6	2997.48	3.92	+0.04	11	0.5(1)			5(2)		4.0(3)	12.3(7)	
51991/2022−025AM	356.6	3010.40	3.94	−1.73	11	2.4(1)			45(3)		1.0(1)	2.1(1)†	
51984/2022−025AE	357.1	3025.10	3.97	−6.38	11				19(2)				
51989/2022−025AK	357.5	3035.99	4.00	−2.99	11				11(2)		1.9(2)	0.6(1)	
51987/2022−025AH	357.9	3047.57	4.02	+1.29	11	3.1(2)			27(3)		0.8(1)	2.0(2)†	
51982/2022−025AC	356.9	3048.97	4.01	−0.12	11	3.6(1)			31(3)		0.9(1)	2.3(2)†	
51980/2022−025AA	356.7	3059.27	4.01	−0.05	11	1.2(1)			38(4)		0.9(1)	1.6(1)†	
51985/2022−025AF	357.1	3069.85	4.02	−0.01	11	2.4(1)			27(3)		1.2(1)	1.3(1)	
51978/2022−025Y	357.1	3080.04	4.02	−0.00	11	3.6(2)			28(2)		1.1(1)	1.1(1)†	
51983/2022−025AD	356.9	3089.36	4.00	−0.05	11	1.5(1)			25(2)		0.8(1)	3.5(2)†	
51981/2022−025AB	356.9	3110.07	3.98	−0.03	11	1.2(1)			16(2)		0.8(1)	2.0(1)†	
51975/2022−025V	357.1	3119.98	3.96	−0.12	11				16(2)				
51976/2022−025W	357.4	3130.23	3.93	−0.06	11	1.0(1)			22(3)		1.2(1)	1.6(1)†	
51972/2022−025S	357.5	3139.86	3.91	−0.05	11				34(4)				
51979/2022−025Z	357.4	3150.16	3.87	−0.09	11	1.1(1)			9(2)		3.3(2)	4.2(3)	
47677/2021−012BK	554.7	3159.90	2.76		1								
51970/2022−025Q	357.4	3160.85	3.82	−0.08	11				27(3)				
51973/2022−025T	357.6	3170.33	3.78	−0.12	11				15(2)				
51968/2022−025N	357.4	3180.57	3.73	−0.12	12				23(2)				
47661/2021−012AT	555.3	3195.27	5.88	−0.02	11	0.8(1)	137(60)	10(1)	50(4)	5(1)	0.3(1)		166(10)
51966/2022−025L	357.8	3200.51	3.60	−0.08	10				22(3)				
51971/2022−025R	357.5	3211.10	3.52	−0.06	10				12(2)				
51964/2022−025J	357.7	3220.55	3.45	−0.04	10				13(2)				
51969/2022−025P	357.7	3230.47	3.36	−0.08	9				20(3)				
51967/2022−025M	357.5	3240.09	3.26	−0.08	8				19(3)				
51962/2022−025G	357.7	3249.53	3.14	+0.09	8				12(3)				
51965/2022−025K	358.1	3260.78	3.04	−0.06	6				18(2)				
51960/2022−025E	358.0	3270.97	2.92	−0.06	6				18(3)				
51957/2022−025B	358.0	3279.97	2.76	−0.03	5							3.0(3)	
51959/2022−025D	357.8	3290.15	2.59	+0.65	4				26(4)				
51963/2022−025H	358.2	3301.21	2.42	−0.10	3				18(5)				
51961/2022−025F	358.0	3310.88	2.21	−0.02	2				17(5)				
51958/2022−025C	358.3	3323.21	1.95	−0.17	1				13(4)			2.1(3)	
51956/2022−025A	358.6	3331.34	1.75		1								
47670/2021−012BC	557.0	3527.13	5.93	+0.05	11	1.0(1)	60(5)	12(1)		4(1)	0.8(1)	0.1(1)	14(2)
45583/2020−025BE	557.0	3565.40	3.26	−0.03	2	0.3(1)	24(6)						168(28)

Notes. Satellites are identified by their NORAD catalogue number and COSPAR-based international designator (which provides the launch year, launch number and sequential identifier). For each satellite, the distance d between the satellite and LOFAR is given at the mid-point of the pass through the 4°.7 FHWM station beam. This midpoint is given by t_{mid}, from the start of the observation at 18:30:00 UTC on 2022 April 1. The duration of the passage of the station beam is given by t_{pass}, while Δt represents the time offset between the predicted and measured time of the pass. The n_{TAB} column indicates the number of tied-array beams the satellite passed through. Detected flux densities S_ν are provided for different frequencies or frequency ranges over the LOFAR observing band. The † symbol indicates that a comb with 50 kHz spacing was detected in the 157 to 165 MHz frequency range.

Table 3. Calibration parameters as explained in the text.

Frequency (MHz)	A_{eff} Station (m^2)	A_{eff} TAB (m^2)	T_{sys} Station (K)	Γ TAB (K Jy^{-1})
125	585	4597	636	1.66
150	512	4021	557	1.46
160	460	3611	500	1.31
175	382	2997	415	1.09

where $\Delta T^{\mathrm{station}}$ is the noise level that can be achieved with a single station based on the radiometer equation. It depends on the system temperature of a station, $T_{\mathrm{sys}}^{\mathrm{station}}$, the number of polarisation channels, $n_{\mathrm{p}} = 2$, that were averaged, the integration time, t_{obs}, and the bandwidth, $\Delta\nu$, which in this case is the width of a spectral channel. The quantity $\Gamma_{\mathrm{tab}} = 0.5 A_{\mathrm{eff}}^{\mathrm{tab}} / k_{\mathrm{B}}$ is the sensitivity or gain that translates between the station level system noise and the TAB flux density RMS. It is determined by the effective aperture area of a TAB, $A_{\mathrm{eff}}^{\mathrm{tab}}$, and the Boltzmann constant k_{B}. The value of $A_{\mathrm{eff}}^{\mathrm{tab}}$ depends on the beam-forming efficiency and the number of contributing antennas. Kondratiev et al. (2016) derived an approximation formula,

$$A_{\mathrm{eff}}^{\mathrm{tab}} = \eta_{\mathrm{active}} N^{0.85} A_{\mathrm{eff}}^{\mathrm{station}}, \tag{4}$$

with the fraction of active dipoles, $\eta_{\mathrm{active}} = 0.95$ (about 5% of the dipoles are typically not in operation), the number of HBA sub-stations in the Superterp, $N = 12$, and the effective aperture area, $A_{\mathrm{eff}}^{\mathrm{station}}$, of one of these sub-stations. van Haarlem et al. (2013) report on the values of $A_{\mathrm{eff}}^{\mathrm{station}}$ for a number of frequencies. For the frequencies used in this paper, we interpolated these values linearly. van Haarlem et al. (2013) also estimated the system equivalent flux density (SEFD), which is the equivalent of the $T_{\mathrm{sys}}^{\mathrm{station}}$ on the flux density scale. The SEFD is relatively constant in the frequency range considered in the following, with a value of about 3 kJy. This can be converted to the system temperature scale using SEFD [Jy] $= 2760\, T_{\mathrm{sys}}^{\mathrm{station}}$ [K] $/ A_{\mathrm{eff}}^{\mathrm{station}}$ $\left[\mathrm{m}^2\right]$ (van Haarlem et al. 2013).

Based on these equations and previously reported quantities, the calibration parameters in Table 3 were determined for use in the subsequent sections. Because the station aperture, $A_{\mathrm{eff}}^{\mathrm{station}}$, appears in both terms, $T_{\mathrm{sys}}^{\mathrm{station}}$ and Γ_{tab}, $\Delta S_{\nu}^{\mathrm{tab}}$ is actually independent on $A_{\mathrm{eff}}^{\mathrm{station}}$. It has a value of 2.986 Jy for all frequencies in Table 3 (a flat SEFD was assumed). In order to calibrate the spectra, it is only necessary to determine the noise level (in arbitrary units) and scale the data such that its RMS equals $\Delta S_{\nu}^{\mathrm{tab}}$.

4.3. Signal detection

Any radio emission associated with Starlink satellites is expected to coincide in time with the predicted passage of a satellite through the LOFAR TABs, though it is a priori unclear if the radio emission would be broad-band, narrow-band, or a combination of both. The search is made difficult, however, as in the LOFAR observing band a lot of active radio services are operated producing signals which could by chance also appear at the same time when a satellite is predicted to pass through the beam.

The band from 110 to 188 MHz under consideration is allocated to several radio services such as air traffic control (118–137, 138–144 MHz), amateur radio (144–146 MHz), emergency pagers (169–170 MHz), satellite transmissions (137–138,

148–150 MHz) and digital audio broadcasting (174–230 MHz), with emergency pagers and digital audio broadcasting being the strongest sources of radio emission (Offringa et al. 2013). The majority of these emission sources are terrestrial and hence are located close to, or on the horizon. As such, these signals will be detected in the sidelobes of the LOFAR station beam and TABs, and hence will appear at the same time and with similar signal strength in all TABs. On the contrary, objects moving through the sky will produce signals in the dynamic spectra of the TABs at different times as they pass through the TABs. This not only applies to the target Starlink satellites, but also to other satellites as well as aircraft.

Based on these considerations, the data-set has been independently searched for signals to avoid biases. We first found a narrow-band signal at 175 MHz and broad-band features with varying intensity spread across the band. Different data processing strategies were applied for this, which apparently were suitable to find the two types of signals. After the first detections were made, it also became clear that some of the satellite positions were not accurately predicted by the ephemerides. However, these first finding made it possible to correct the positional data, which triggered additional detections at further frequencies. In the following we provide a summary of the process.

Most of the brighter broad-band signals were already visible in the raw, uncalibrated dynamic spectra of the TABs after binning; see Fig. 6. As the duration of a pass through a TAB is of order 0.1 to 0.6 s, the dynamic spectra were averaged to a time resolution of 41.94 ms, keeping the frequency resolution fixed to 12.21 kHz. Next, AOflagger (Offringa et al. 2012) was used with the standard LOFAR flagging strategy to identify non-astrophysical signals and create a mask for the dynamic spectrum of each TAB. We found that, on average, 23% of the dynamic spectrum is flagged, 6.25% of which is due to each 16th channel, which contains the DC component of 16 channel poly-phase filter-bank used to channelise the LOFAR 0.195 MHz sub-bands into 12.21 kHz channels.

For each Starlink satellite passing through the LOFAR station beam, we started by extracting 20 s in time centred on the predicted mid-point of the pass through the LOFAR station beam from each of the 91 TABs. For this we used the band-pass calibrated dynamic spectra. To minimise the impact of terrestrial signals, which often appear similar in all beams, we subtracted from the extracted dynamic spectrum of each TAB the mean of the dynamic spectra of all the other TABs. Finally, again for each satellite pass, the resulting dynamic spectra of those TABs through which the satellite passed were aligned in time based on the predicted passage time and averaged to increase the signal-to-noise of any satellite emission. We note that with this approach we specifically chose not to mask any data that was flagged by AOflagger, this was to ensure that no emission from satellites would be removed from the analysis.

Inspection of these averages of TABs showed broad-band emission throughout the observed frequency range, coinciding with the crossing times of Starlink satellites. Normalised, aligned, and averaged dynamic spectra for two satellites are shown in Fig. 7. The dynamic spectra have a time resolution of 41 ms and the full frequency resolution of 12.21 kHz. Due to the normalisation with the dynamic spectra of the other TABs, bright signals in those TABs may lead to depressions in these plots. To prevent masking of signals associated with satellites, no masking has been applied when normalising, aligning and averaging these spectra. Not all satellites reveal broad-band emission at the same frequencies – the two most common frequency
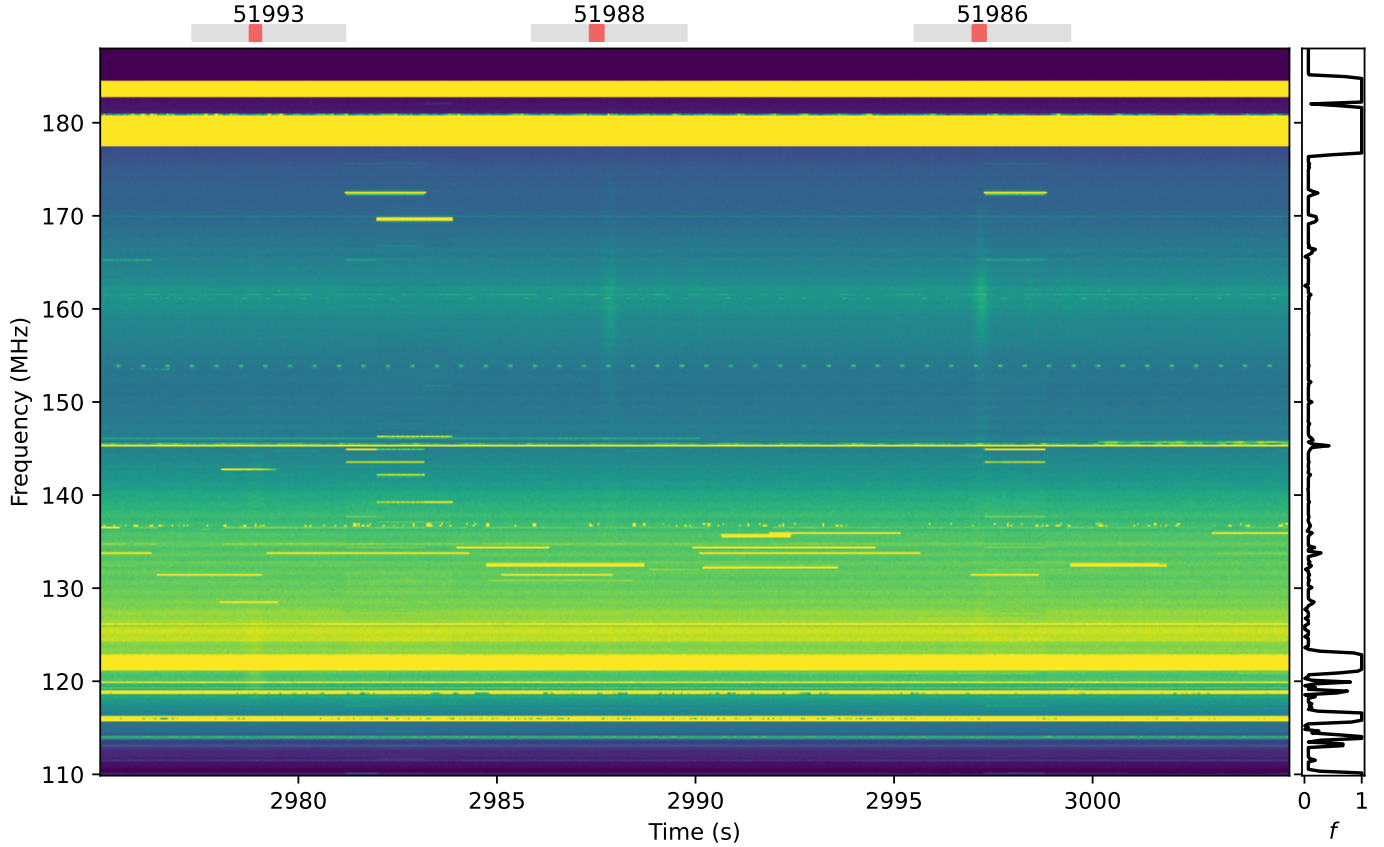
Fig. 6. Dynamic spectrum of tied-array beam 18, showing broad-band radio emission of three Starlink satellites (NORAD IDs 51993, 51988 and 51986) coincident with the predictions from satellite ephemerides. For NORAD ID 51993, the emission is visible from 115 to 130 MHz, while objects 51988 and 51986 are more obvious from 140 to 175 MHz. The dynamic spectrum has been averaged by a factor four in time to a time resolution of 41 ms, and a factor 16 in frequency to a frequency resolution of 0.195 MHz. To show the temporal and spectral structure of the satellite emission, as well as that of other anthropogenic signals, the raw, uncalibrated dynamic spectrum is shown, without masking of anthropogenic signals. The bars at the top of the dynamic spectrum indicate the predicted time ranges where the indicated satellite passed through the LOFAR station beam (in grey), and the specific tied-array beam (in red). In the case of object 51988, the emission is about 0.33 s delayed compared to the prediction. The histogram on the right shows the fraction of the dynamic spectra that would have been masked in frequency by `OAflagger` (Offringa et al. 2012).

ranges where emission is detected are at 116–124 MHz and 157–165 MHz. We focus our analysis on these two frequency ranges, but also include the ITU-R RAS frequency band from 150.05 to 153 MHz.

Besides broad-band emission, narrow-band emission was also detected in, and confined to, several individual 12.21 kHz channels. The frequencies of these channels cover 124.994 to 125.006 MHz, 134.991 to 135.004 MHz, 143.048 to 143.060 MHz, 149.994 to 150.006 MHz and 174.994 to 175.006 MHz. We include these signals in our analysis, and will refer to them as the narrow-band emission at 125, 135, 143.05, 150 and 175 MHz. As the maximum radial velocities of the Starlink satellites in this observation are less than $|v_{\rm r}| < 1 \, {\rm km\,s^{-1}}$, any Doppler shifts at these frequencies are less than ~ 600 Hz and hence confined to individual spectral channels.

As shown in Fig. 7, the signal strength of these narrow-band emission can vary significantly between frequencies as well as satellites. In some cases, the narrow-band features were so bright, that the satellite was detected passing through the sidelobes of individual TABs. Furthermore, in many cases, especially at 125 MHz, the narrow-band signals were superposed with terrestrial signals. This is also why the data processing strategy had to be modified in order to extract the narrow-band signals properly. Instead of subtracting the average of all beams

from each spectrogram we subtracted a spectral baseline in a small window around each narrow-band peak.

Finally, in some, but not all, of the lower altitude Starlink satellites, a comb of narrow (within a 12.21 kHz channel) peaks was seen in the frequency range above 155 MHz. The dynamic spectra of satellite 51998 shown in Fig. 7 shows this comb for frequencies between 170 and 176 MHz. Power spectra of the emission between 157 to 165 MHz shows that these peaks are spaced at 50 kHz offsets and is detectable in 17 of the 46 satellites at lower altitudes, but none of the higher altitude satellites. The satellites where this comb was detected are marked in Table 2.

For all satellites which were detected through either broad-band or narrow-band emission, we determined the time offset between the observed and the predicted passage time through the TABs by fitting a Gaussian profile to the temporal emission profiles. These time offsets are listed in Table 2. We found that the time offsets are less than 1 s for all but four satellites, and excluding those yields a median time offset of $\bar{\Delta}t = -0.03 \pm 0.14$ s. The four satellites with the largest time offsets passed through the beam pattern by as much as 6.4 s earlier, and others 1.3 s late compared to predictions. We furthermore found that the temporal width of the Gaussian fits matches those from predictions, where the satellites at 350 km orbital altitudes moved through
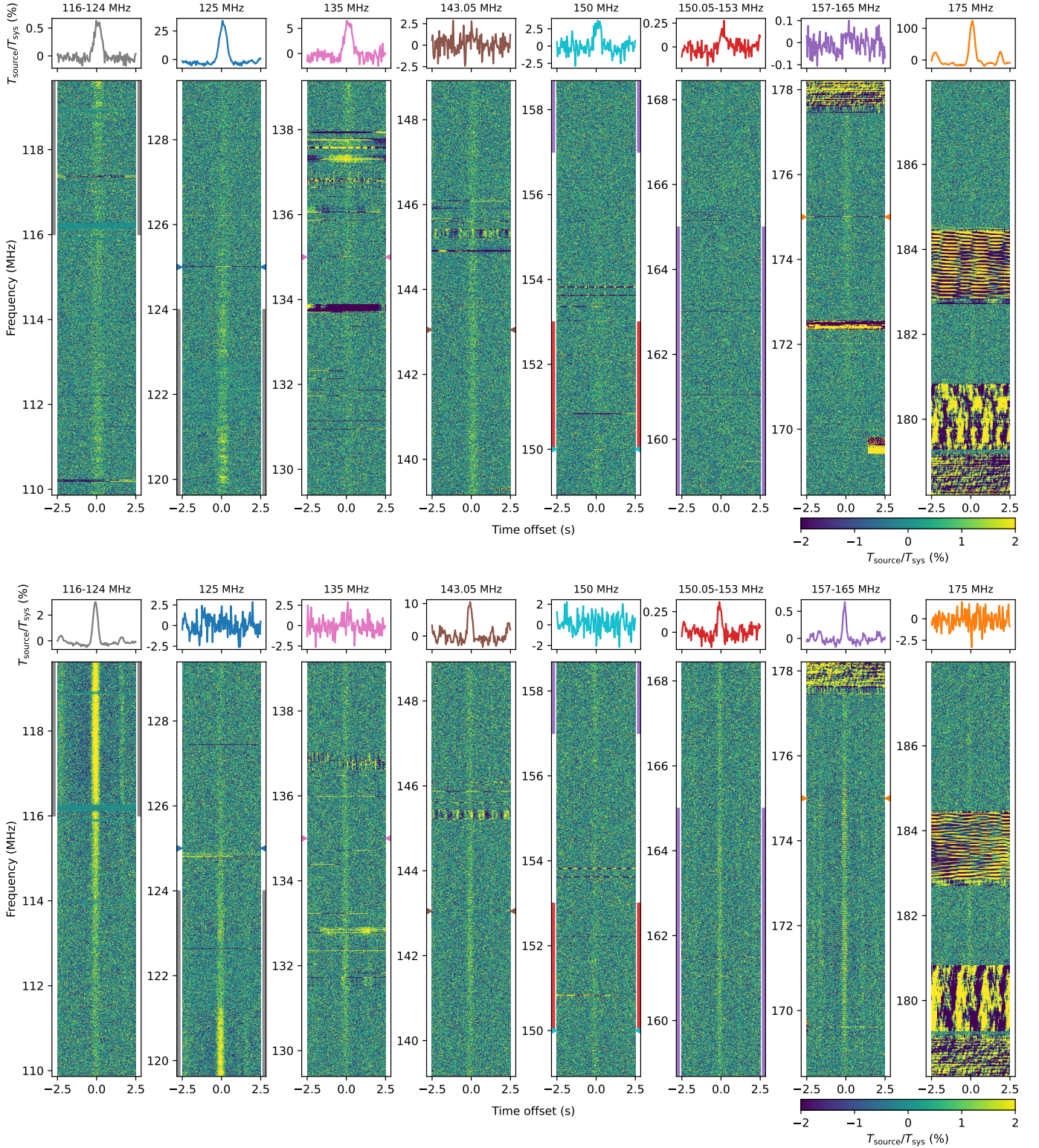
Fig. 7. Spectral and temporal properties of the passes of satellites 45186 (average of 11 TABs) and 51998 (average of 10 TABs). For each satellite pass, normalised, aligned and averaged dynamic spectra are shown over the entire observed bandwidth and within 2.5 s on the predicted passage time. Time series at narrow-band frequencies of 125, 135, 143.05, 150, and 175 MHz are shown in the top insets, as well as for broad-band frequency ranges (116 to 124, 150.05 to 153, and 157–165 MHz). The colour of each time series matches the marked frequencies and frequency ranges in the same colours to the sides of the dynamic spectra. For both satellites a combination of broad-band and narrow-band emission is visible. In the case of satellite 45186, broad-band emission is mostly confined to the frequencies below 155 MHz, but narrow-band emission at 125, 135, 150, and 175 MHz is detected, with sidelobes being visible at 175 MHz. Some structure in the broad-band emission is obvious between 120 and 122 MHz. For satellite 51998, broad-band emission is clear at all frequencies not affected by terrestrial signals, while narrow-band emission is absent, except for 143.05 MHz. Between 170 and 176 MHz, a comb of narrow-band, regularly spaced peaks, is superposed on the broad-band emission. The temporal profiles show time offsets of the observed satellite pass with respect to predictions (+0.09 s for 45186, −0.07 s for 51998).
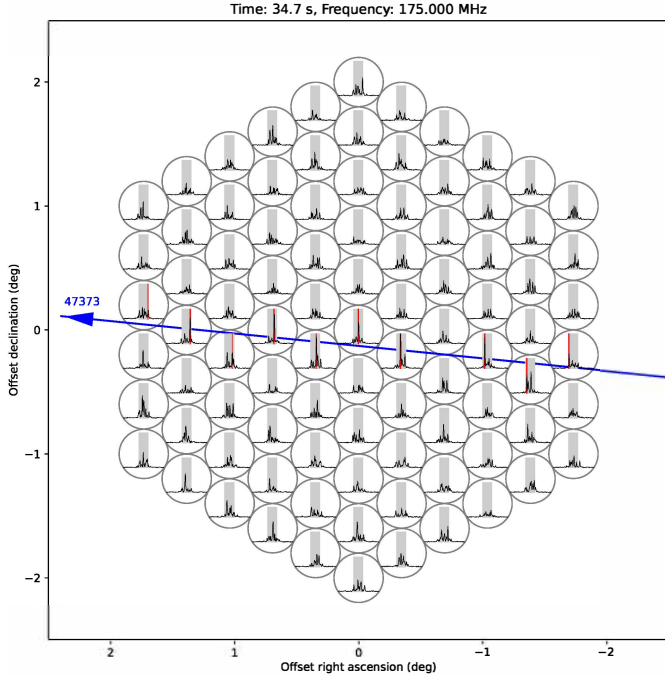
Fig. 8. Visualisation of the detected signal from satellite 47373 as it crossed the field of view of the LOFAR tied array beam pattern. Each circle marks one of the beams. The inlays show the 175 MHz signal (spectral PFD) as a function of time spanning about ∼20 s centred around the event time (approximately 35 s after observation start). The grey-shaded areas mark the total time interval over which the satellite was in the field of view, the red shaded areas refer to the time when the satellite was in the corresponding beam area.

Fig. 9. As Fig. 8 but for satellite 45705.

Fig. 10. As Fig. 8 but for satellite 51978 visualising a broad-band signal in 116–124 MHz.

the beam faster than those at 550 km. Subsequently, all these offsets were used to modify the satellite ephemerides and further analyses were based on the corrected positions.

To visualise the emission as a satellite passes through the LOFAR TAB beam pattern, Figs. 8–10 show the temporal profiles of satellite passes in comparison to the location of the satellite as it passes through the beam pattern. The case of satellite 47373 shown in Fig. 8 is one of example for a very bright event, where the narrow-band emission at 175 MHz was strong enough to be detected in all TABs for the full duration that the satellite passed through the 4°.7 FWHM station beam. In other cases, such as for the pass of satellite 45705 (Fig. 9) the behaviour was 'normal', however, and a signal was only detected in the beams covering the satellite sky track. For completeness, also an example for the broad-band emission between 116 to 124 MHz is displayed in Fig. 10 for the pass of satellites 51978. As expected, the strongest detections coincide with the predicted time that the satellites passed through the individual TABs, confirming that the signal was coming from the direction of the satellites.

Next, we used the intensity-calibrated spectra to estimate the power flux densities (PFD) for each one of the detected signals. As the satellites usually did not cross any of the beam centres exactly, we determined the PFD as a function of the angular separation between the satellite positions with respect to each of the TAB centres; see Fig. 11 for two example satellites. Based on a Gaussian least-squares fit to the data points, the peak PFD could be estimated. These PFD measurements are provided in Table 2. Furthermore, a visual overview is provided in Fig. 12. It is noteworthy that for the events with very high intensity (above about 100 Jy) the Gaussian fit was made difficult because of
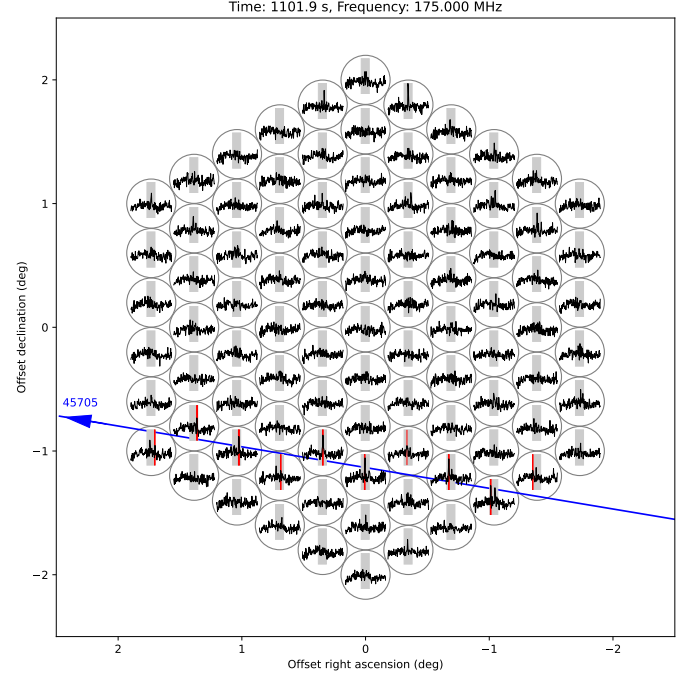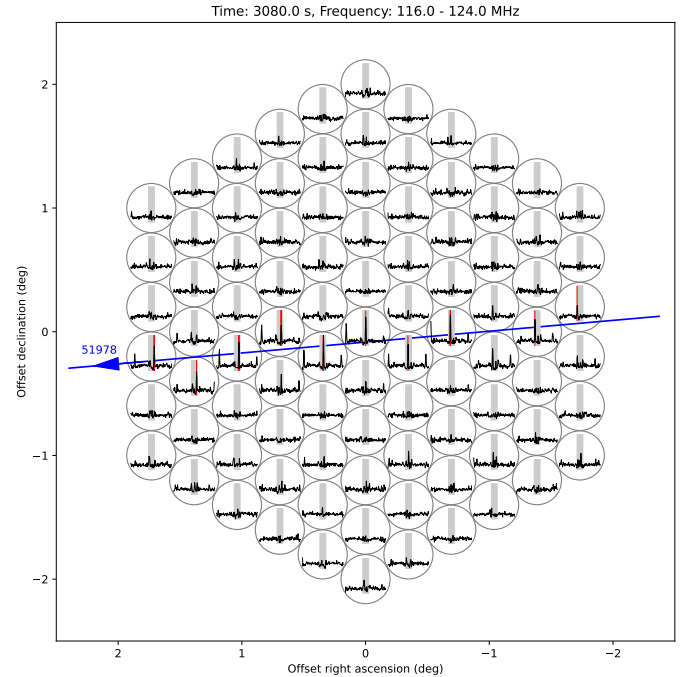
the cross-talk induced by the LOFAR beam-former (e.g. Fig. 11 left panel). Therefore, the width parameter of the Gaussian fit curve was constrained to values below $1.1\vartheta_{\mathrm{fwhm}}^{\mathrm{tab}}$. Likewise, for all fits the zero level offset was constrained to values close to zero. Also, the scatter in the flux density values was rather large, such that the accuracy of the S_ν values in Table 2 should not be overestimated.
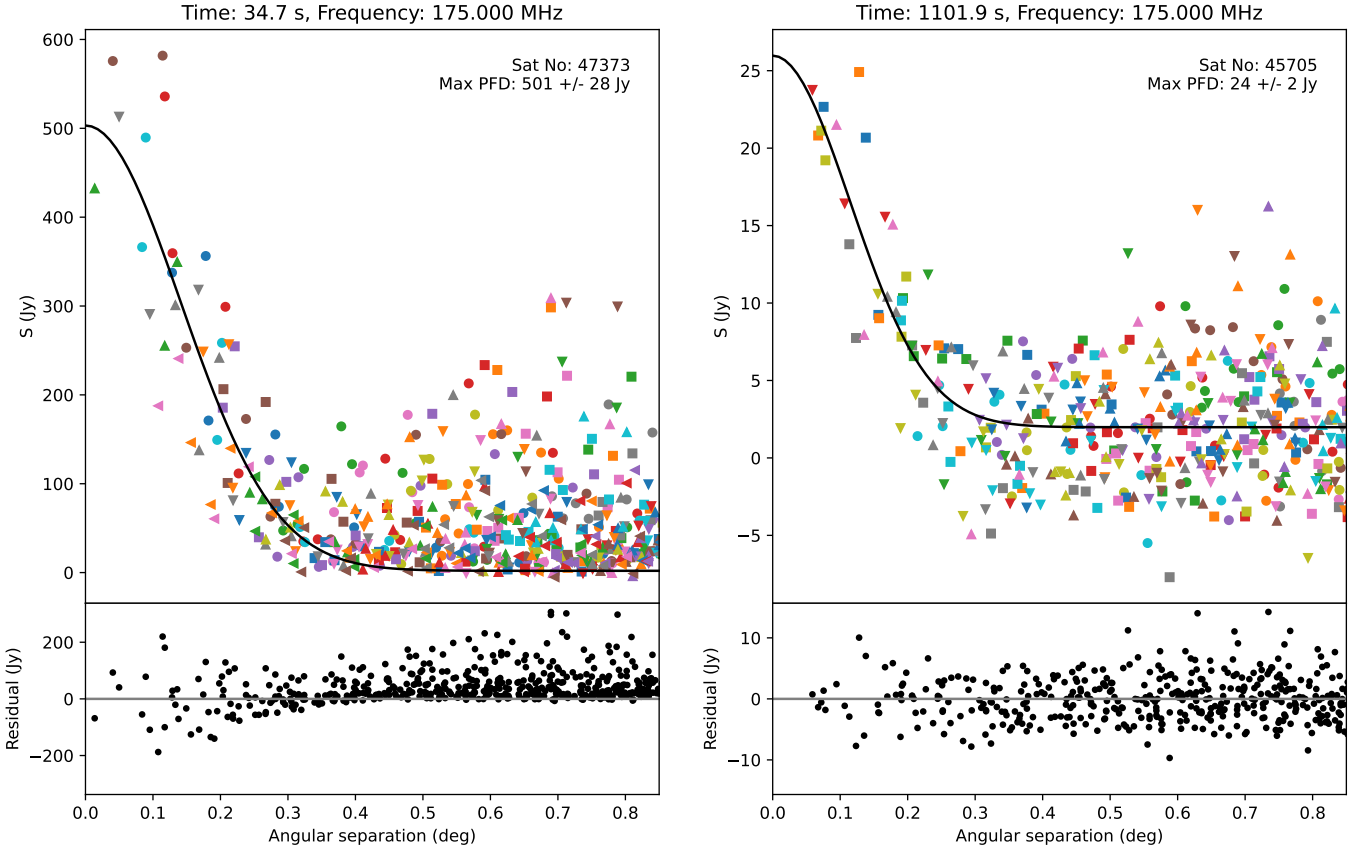
Fig. 11. Measured spectral power flux densities for satellites 47373 and 45705 as a function of angular separation from beam centres. Different colours and symbols mark different beams. The black solid line represents a least-squares fit (Gaussian function) to the data points. This allows to estimate the actual spectral PFD of the satellite, which is about 460 Jy (47373) and 25 Jy (45705), respectively, averaged over one spectral channel of 12.2 kHz at 175 MHz.
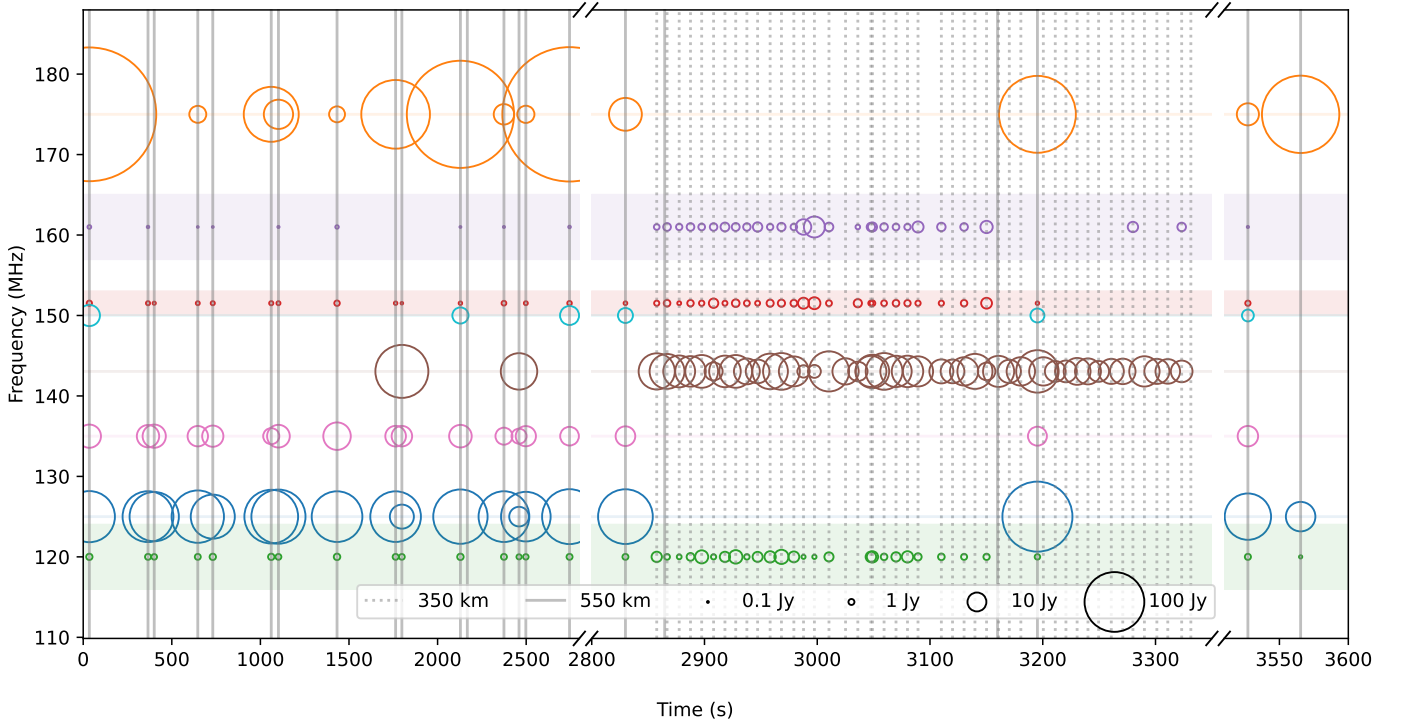

Fig. 12. Radio emission detected from Starlink satellites during the LOFAR observation. Passes of Starlink satellites through the LOFAR beam pattern are marked in time with solid vertical lines for satellites at $h = 550$ km, and dotted lines for those at $h = 350$ km. The coloured horizontal lines and bands indicate the frequencies of frequency ranges in which fluxes were measured, with the circles indicating the corresponding flux density measurements.

5. Analysis of the detected events

5.1. Signal properties

Using the flux density measurements of satellite events at the narrow- and broad-band frequencies as listed in Table 2 we can infer some properties of the detected signals.

We found that the narrow-band emission at 125, 135, 150, and 175 MHz is only detected for the Starlink satellites at their operational altitude of $h = 550$ km, and not seen in any of the Starlink satellites in the lower orbit at altitudes of $h = 350$ km. As the higher altitude satellites are more distant ($d \sim 555$ km) compared to the lower altitude satellites ($d \sim 356$ km), any emission of equal intensity should cause a detection in the received data about $(555 \text{ km}/356 \text{ km})^2 \sim 2.4$ times brighter for the satellites at lower altitudes. While the individual satellites showed some variation in the signal strengths, it is deemed extremely unlikely that all of the lower altitude satellites would by chance have very low emission. Hence, it naturally appears that there is an intrinsic difference between the satellites in higher altitude and lower altitude orbits with respect to the narrow-band features.

This is not the case for the broad-band emission, which was detected for the majority of satellites, regardless of their orbital altitude. We found that the median PFD of the low altitude satellites is a factor 2.0 and 2.3 higher than that of the high altitude satellites for frequency ranges of 116 to 124 MHz and 150.05 to 153 MHz, respectively. As this is close to the expected factor of 2.4, this indicates that the generation of this emission is independent on altitude. Curiously, the broad-band emission between 157 and 165 MHz is a factor 15 higher in the low altitude satellites, suggesting an intrinsic difference in this frequency range.

The occurrence of the signals for individual satellites at different frequencies is correlated. For 18 out of 19 cases in which narrow-band emission at 125 MHz was detected, emission was also present at 135 MHz, albeit somewhat fainter. A similar relation exists between the emission at 125 MHz and 175 MHz, though the emission at 175 MHz appears to be more variable and can be brighter than at 125 MHz. The signal at 175 MHz was detected in 14 cases. The narrow-band emission at 150 MHz was only seen for those satellites that were very bright at 175 MHz (and cross the station beam) and was detected in six cases.

As the lower altitude satellites were still in the orbit-raising phase, the 125 and 175 MHz might be associated with the regular operation (e.g. communication-link transmissions) of the satellites. Also, both frequencies are odd multiples of 25 MHz – a frequency often used for local oscillators – and could be harmonics, which usually appear stronger at either odd or even multiples of the fundamental mode. This would also explain, why the 150 MHz signal is only present for the brightest of the 175 MHz detections (as 150 MHz is an even multiple of 25 MHz). Typically, square wave-like signals are expected to produce odd harmonics. It is unclear, how the 135 MHz feature would fit into this. It might be owing to some intermodulation product of the detected narrow-band features with some other signal, but we were not able to find further evidence for this.

We attribute the narrow-band emission detected at a frequency of 143.05 MHz to the GRAVES space surveillance radar (Michal et al. 2005). The GRAVES transmitter is located 30 km east of Dijon, France and is known to transmit continuous wave signals at 143.050 MHz for bi-static Doppler tracking of satellites. The transmitter illuminates a 180° range in azimuth (east to west through south) and a 30° range in elevation (Jouade &

Barka 2019). Though the radiated power of the transmitter is not publicly known, radar reflections from meteors are regularly detected by radio amateurs using modest equipment, even for meteors located well outside of the nominal illumination pattern of the GRAVES transmitter (e.g. Fleet 2015). The Starlink satellites that we observed were also located far outside of the (known) GRAVES illumination area, implying that even in the far sidelobes of the GRAVES radar the effectively transmitted power is substantial.

Another interesting finding is that most high-altitude satellites do not show GRAVES reflections, even though LOFAR should have the sensitivity to detect them. The two satellites that were detected at 143.05 MHz were even brighter than the low-altitude satellite reflections (when they should be weaker owing to longer propagation paths). This suggests that the details of the propagation are subject to several effects, the magnitude of which cannot easily be determined without additional information. One aspect is certainly the orientation of the satellite relative to the LOFAR station. It is known that Starlink uses the 'open-book' mode during orbit raising, where the solar array is aligned parallel to the satellite body to reduce atmospheric drag, while the operational satellites are in 'shark-fin' configuration, where the solar array is located mostly behind the satellite as seen from Earth. Furthermore, the exact path geometry is expected to differ between lower and higher orbit altitudes, as well as the side-lobe gain of GRAVES towards different elevations.

5.2. Assessment of transmitted power levels

The maximum detected spectral power flux densities were about 500 Jy (average over one spectral channel) for the narrow-band signals and of the order of a few Jy for the broad-band signals. As the distance to the satellites, d, and the main beam gain of the HBA TAB are known, it is possible to determine the transmitter spectral EIRP (equivalent isotropically radiated power), P_ν^{tx}. The EIRP is the power that a transmitter with an isotropic antenna would have to radiate to produce the observed signal. As the transmitter antenna pattern, G_{tx}, and pointing direction are unknown, it is not possible to infer the conducted power at the antenna port of the satellite. The conversion formula between spectral EIRP and measured power flux densities is given by

$$S_\nu = G_{\text{tx}}(\vartheta, \varphi) \frac{P_\nu^{\text{tx}}}{4\pi d^2} \stackrel{G \cong 1}{=} \frac{P_\nu^{\text{tx}}}{4\pi d^2}, \tag{5}$$

assuming only line-of-sight propagation loss and neglecting other effects, such as atmospheric attenuation. The resulting minimum and maximum spectral EIRP values for each band are compiled in Table 4, providing results for low- and high-altitude satellites separately.

The transmitted EIRPs can also be converted to electric field strengths to make comparison with EMC standards simpler; compare Sect. 3.2. The corresponding values are also provided in the table. For the narrow-band signals at 125, 135, 143, 150, and 175 MHz, respectively, electric field strengths in the range of 24 to 49 dB $\left[\mu\text{V m}^{-1}\right]$ are determined, normalised to what an average detector with bandwidth of 120 kHz at a distance of 10 m would measure. The typical values for the broad-band signals are between 21 and 39 dB $\left[\mu\text{V m}^{-1}\right]$, again for a 120 kHz detector bandwidth.

These values can be compared with the results of the EPFD simulations in Sect. 3.3, in particular with Table 1. In the EPFD

Table 4. Derived satellite transmitter parameters for the weakest and brightest detections.

Frequency (MHz)	Type	Altitude (km)	$P_\nu^{\text{tx,eirp}}$ (dB[W Hz^{-1}])		E-field[1] (dB[µV m^{-1}])			
					$\Delta f_{\text{det}} = 120$ kHz		$\Delta f_{\text{det}} = 2.95$ MHz	
			min	max	min	max	min	max
116–124	broad-band	~360	−141	−130	24	35	38	49
	broad-band	~550	−139	−133	26	32	40	46
125	narrow-band	~360						
	narrow-band	~550	−124	−113	32	43	32	43
135	narrow-band	~360						
	narrow-band	~550	−126	−121	30	35	30	35
143	narrow-band	~360	−132	−121	24	34	24	34
	narrow-band	~550	−118	−115	37	40	37	40
150	narrow-band	~360						
	narrow-band	~550	−128	−123	28	33	28	33
150.05–153	broad-band	~360	−142	−132	24	34	38	48
	broad-band	~550	−141	−135	24	31	38	45
157–165	broad-band	~360	−140	−127	25	39	39	52
	broad-band	~550	−145	−138	21	27	35	41
175	narrow-band	~360						
	narrow-band	~550	−126	−107	30	49	30	49

Notes. [1] As measured with an average detector at a distance of 10 m with given detector bandwidths, Δf_{det}.

simulations it was however assumed that a signal had a constant electrical field strength over the full allocated RAS band 150.05−153 MHz. All electrical field values have also been converted to a measurement bandwidth of 2.95 MHz which fully covers the RAS band for the convenience of comparison. They are provided in the right-most column of Table 4. It is noted that for narrow-band signals the values are the same for both detector bandwidths (120 kHz and 2.95 MHz), because the total integrated power is the same, while for a broad-band signal the total power increases, the more bandwidth is considered. The range of field strengths for the measurement bandwidth of 2.95 MHz is thus 24 to 49 dB $\left[\mu\text{V m}^{-1}\right]$ (narrow-band) and 35 to 52 dB $\left[\mu\text{V m}^{-1}\right]$ (broad-band)

For the detected Starlink satellites, Table 1 cites maximum E-field values of 25.6 and 23.8 dB $\left[\mu\text{V m}^{-1}\right]$ given a measurement bandwidth of 2.95 MHz for the (effective) antenna diameters of 25 and 70 m, respectively. Hence, even the weak detections exceed the suggested limit, while the brightest detections are more than 20 dB above the limit.

It has to be emphasised, though, that our observations represent only a snapshot, measuring a small sub-set of all satellites and that the detected signals are not equally bright and some satellites did not even reveal UEMR at certain frequencies. Nevertheless, the overall number of detections indicates that satellite-borne UEMR from large satellite constellations could indeed be an issue for RAS operations.

5.3. Intrinsic emission or reflection?

Theoretically, it is possible that the measured signals do not originally stem from Starlink satellites but are of terrestrial origin, reflected off the satellites. To test this hypothesis, we first determine whether a terrestrial signal could only be visible as reflection, but not over the direct terrestrial path. Second, the transmitted power level is estimated, which would be required to create a signal of the observed properties.

5.3.1. Geometrical considerations

Before the link budgets of both propagation paths can be compared, the geometry of the paths needs to be worked out. The highest likelihood that a terrestrial transmitter at distance d from the RAS station is not seen, while the reflected signal is visible, is given when d is as large as possible compared to transmitter−satellite and satellite−receiver distance, d_1 and d_2 respectively. This is the case, when all three objects (transmitter, satellite, and receiver) are in a plane perpendicular to the ground. It is noted that none of the paths actually follow straight lines. The terrestrial path, d follows a geodesic, while d_1 and d_2 are subject to refraction (which was not considered in this analysis).

In Fig. 13, the path geometry is analysed for the high- and low-altitude satellites. It is assumed that the satellite appears at an elevation angle of 85 deg from the LOFAR observer. Based on the azimuthal angle of the satellite (with respect to LOFAR) one can construct a geodesic[18] starting at the LOFAR observer out to a certain distance. Along this path, one can put a hypothetical transmitter and determine under which elevation angle the same satellite would appear in the transmitter frame (topocentric). Likewise, the geodesic distance (i.e. the projection on the ground) between transmitter and satellite can be inferred. The latter two quantities are shown in Fig. 13 as red and blue curves, respectively. At about 2000 km distance, the low-altitude satellite would be set below the horizon.

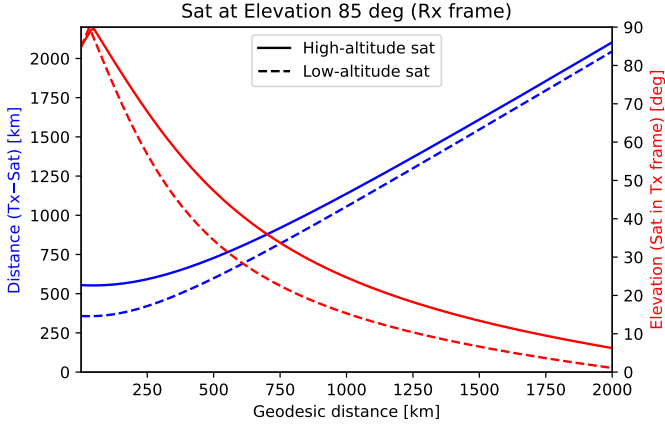[18] For simplicity, the Earth Ellipsoid WGS-84 is assumed.

Fig. 13. Geometry of the satellite reflection scenario.

Fig. 14. Path propagation losses of the satellite reflection scenario vs. the direct terrestrial (trans-horizon) path loss. The red line indicates the distance (~ 620 km of the GRAVES radar from the LOFAR observer.

5.3.2. Link budgets

The propagation losses for both paths are determined by different physical processes. In the terrestrial case, the diffraction on the spherical Earth, tropospheric scatter, and other effects play a role. The model proposed in Rec. ITU-R P.452-17 is employed to calculate the loss, $L_{\text{terr}}(d)$. For the effective propagation loss, also the antenna gains need to be considered:

$$\frac{P_{\text{rx}}}{P_{\text{tx}}} = G_{\text{tx}}G_{\text{rx}}L_{\text{path}}^{-1}. \tag{6}$$

In the line-of-sight case (which is not relevant here), one would find[19]

$$L_{\text{terr}}(d) \approx \left[\frac{4\pi d}{\lambda}\right]^2, \tag{7}$$

It should be pointed out that we follow the common practice of spectrum management and many other fields, to define the loss as a quantity larger than 1 (i.e. positive on the Decibel scale).

Unfortunately, it is not known, what the antenna gains towards the local horizon are for both, transmitter and receiver. Therefore, we have to assume values. The most simple choice is to set both gains to 0 dBi.

For the reflection scenario, the Radar equation has to be used:

$$P_{\text{rx}} = \frac{P_{\text{tx}}G_{\text{tx}}}{4\pi d_1^2}\sigma_{\text{rc}}\frac{1}{4\pi d_2^2}A_{\text{eff}}^{\text{rx}}, \tag{8}$$

and we can express this in a similar way as Eq. (6):

$$\frac{P_{\text{rx}}}{P_{\text{tx}}} = G_{\text{tx}}G_{\text{rx}}\left[\frac{4\pi}{\lambda^2}\right]\left[\frac{\lambda}{4\pi d_1}\right]^2\sigma_{\text{rc}}\left[\frac{\lambda}{4\pi d_2}\right]^2$$
$$\equiv G_{\text{tx}}G_{\text{rx}}\left[\frac{4\pi}{\lambda^2}\right]L_{\text{sky}}^{-1}(d_1)\sigma_{\text{rc}}L_{\text{sky}}^{-1}(d_2). \tag{9}$$

Here, the radar cross section, σ_{rc}, was introduced. For Starlink, we assume $\sigma_{\text{rc}} = 10$ m^2 as we are not aware of a publicly available measurement. The effective cross section also depends on the orientation of the satellite and the frequency range considered. Note, that for a mono-static Radar, $d_1 = d_2 = d$, and thus the propagation loss would scale with distance to the fourth power. In our case however, d_1 and d_2 can be very different.

---

[19] Because $P_{\text{rx}} = S \cdot A_{\text{eff}}^{\text{rx}} = \frac{P_{\text{tx}}G_{\text{tx}}}{4\pi d^2}A_{\text{eff}}^{\text{rx}}$ and $A_{\text{eff}}^{\text{rx}} = G_{\text{rx}}\frac{\lambda^2}{4\pi}$.
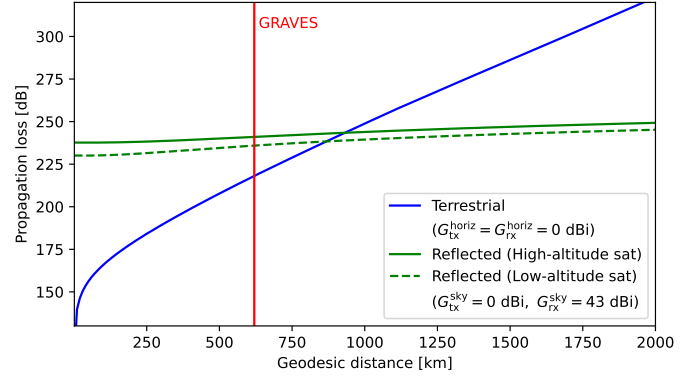
Figure 14 displays the path propagation losses of the satellite reflection scenario vs. the direct terrestrial (trans-horizon) path loss. It has to be noted that for the terrestrial path, neither the terrain (such as hills) nor clutter was accounted for. Both can add substantial additional path propagation losses of 20 dB and more, each. In the reflection case, the LOFAR TAB points at the satellite, such that the full main beam gain applies (43 dBi at 175 MHz). Again, without further knowledge it is assumed that the transmitter gain towards the satellite is 0 dBi. Under these assumptions, the propagation path over the reflection off the satellite would be more efficient beyond about 900 km compared to the terrestrial propagation. At this distance the satellite would appear at approximately 20–25° elevation in the transmitter frame. If the transmitter signal would be targeted towards the satellite, then the antenna gain, $G_{\text{tx}}^{\text{sky}}$ would be much higher than the assumed 0 dBi, which would further decrease the distance at which the reflection scenario is more efficient. Likewise, diffraction at terrain or clutter losses would also increase the terrestrial path loss and make the reflection scenario more efficient.

5.3.3. Estimating the transmitter power (reflection scenario)

The calculations above show that it is indeed possible for a transmitter to create a stronger reflected signal than over the direct terrestrial path, once the distance between transmitter and receiver gets large enough. This is a consequence of the large diffraction loss on the trans-horizon terrestrial path. But still, the propagation loss via the satellite reflection is very high, so it may be interesting to estimate the required transmitter power. Again, as the transmitter antenna gain is unknown, we can only calculate the EIRP (towards the satellite), but not the conducted power at the antenna port of the transmitter.

Based on the reflected-case path propagation loss in Fig. 14 and the maximum received narrow-band power of

$$P_{\text{rx}} = A_{\text{eff}}^{\text{tab}}S_\nu\Delta f = 2997 \text{ m}^2 \cdot 506 \text{ Jy} \cdot 12.2 \text{ kHz} = -157 \text{ dB[W]}, \tag{10}$$

the transmitter power (EIRP towards satellite) would need to be between 81 and 92 dB[W] or 73 and 88 dB[W] for high- or low-altitude satellites, respectively, depending on the distance between radar transmitter and satellite. This is a huge number and would require a LOFAR-size transmitter with a conducted power in the kilo-Watts regime (concentrated within a bandwidth

of only 12.2 kHz)[20]. In the case of the GRAVES frequency, it is indeed very likely that the detected signal is in fact originating from the GRAVES radar and reflected off the satellites. GRAVES probably has sufficient transmit power to explain the received signals. In fact, there are numerous reports by amateurs who receive GRAVES signals that were reflected by meteors with small receiving antennas. The distance between GRAVES in the eastern part of France and the LOFAR superterp is about 620 km. This is large enough to make the reflection path more efficient than the direct terrestrial path, as for LOFAR the local clutter environment will play a role and there is also relatively hilly terrain along the propagation path in France and Belgium that would increase the diffraction losses.

No other radar facility is known that operates at the detected frequencies. While for these cases, the radar scenario cannot be fully excluded, we find it unlikely. The fact that the 125 and 175 MHz signals were only observed for the higher orbit satellites is another aspect that would be hard to explain within a radar scenario. And a powerful radar that would operate broad-band between about 110 and 170 MHz would probably be well-known as it would interfere with many applications in a large area around the transmitter.

6. Summary and conclusions

Using the LOFAR radio telescope, we have detected radiation between radio frequencies of 110 and 188 MHz that is correlated with satellites of the SpaceX/Starlink constellation. These frequencies are well below the assigned transmission frequencies at 10.7–12.7 GHz. Broad-band emission was present over the whole observed bandwidth for some satellites, while others showed strong (from 10 Jy up to ∼500 Jy) narrow-band signals at frequencies of 125, 135, 150, and 175 MHz. The presence of narrow-band emission differs between Starlink satellites at operational altitudes with those that were still actively raising their orbits, indicating possible differences in the operational state of the satellites, or differences between their hardware versions. We found that the flux density of the broad-band emission decreases with range, suggesting this emission is likely intrinsically generated and is detectable in 47 of the 68 Starlink satellites that were observed. However, narrow-band radio emission at 143.05 MHz can be attributed to reflections of transmissions from the French GRAVES space surveillance radar, and while we know of no other radars operating at the detected narrow-band frequencies or broad-band frequency ranges, confirmation that the observed narrow-band emission at other frequencies is intrinsic is required.

The narrow-band emission detected at 125, 150, and 175 MHz may be harmonically related, suggesting a local oscillator or clock signal operating at a frequency of 25 MHz. It is noteworthy that the narrow-band signals were only detected for satellites at the operational altitude. No such signals were seen for the satellites in orbit-raising phase, it is unclear if this effect is owing to operation or satellite version. The broad-band features are with high probability caused by other means, such as switched-mode power supplies, communication signals internal to the satellites, or some other electronic or electrical subsystem.

Follow-up observations will be able to shed further light on the origin and properties of the observed emission. Observations with the LOFAR Low-Band Antennas (LBAs; 10–90 MHz) would be able to confirm the presence of a 25 MHz local oscillator, while higher frequency resolution observations should allow the distinction between intrinsic or reflected emission from the Doppler shifts of the narrow-band emission. Further observations with LOFAR as well as other radio telescopes will be required to investigate the properties of the emission between different Starlink satellite versions at operational altitudes, if the emission changes when the satellites are in the Earth's shadow and the solar array is not illuminated by the Sun, and if radio emission from Starlink satellites is detectable at higher radio frequencies. Besides further observations of satellites from the Starlink constellation, it would be prudent to determine if satellites from other constellations emit UEMR. Finally, the impact of – and possible mitigation strategies against – the observed emission from satellites of the Starlink, or any other, constellation on the different science cases of LOFAR and other current, as well as future, radio observatories (e.g. MWA, LWA, SKA1-Low) operating at low frequencies needs to be investigated.

Any kind of UEMR is not subject to spectrum management of active radio services. In fact, from the radio astronomers perspective, UEMR is currently not well regulated for satellites and spacecraft. While there are some electromagnetic compatibility standards for spacecraft, these were made to protect the subsystems within a spacecraft from each other or its launcher system, but not to protect third party activities. The measurements presented in this paper show that there is a potential for harmful interference (as defined in the ITU-R radio regulations using the RA.769 thresholds) in radio astronomy observations caused by satellites in frequency bands far away from their allocated carrier frequencies. This potential is a function of the number of satellites and their orbital parameters, thus large satellite constellations may pose a risk. A big difference between wanted transmissions via antennas and UEMR, is that the latter is most likely not directional but relatively isotropic. Therefore, one important protection measure, which is to exclude radio astronomy stations from the service area of a satellite network, is not possible for UEMR. In addition, a strong terrestrial transmitter, which is not immediately an issue because of good geographical separation, can produce reflected signals via the satellites' surfaces. A sphere of satellites could produce a new propagation channel which may need to be considered in terrestrial radio-propagation models as the ones developed by the ITU, this requires further study. Both effects, intrinsic and reflected emission, are presently not considered in the national and international regulation processes.

Because the detected signals in our 1-h observation represent only a snapshot and a small fraction of the Starlink constellation, one can currently not estimate accurately if and how much an entire satellite constellation, Starlink or other, would exceed protection thresholds in RAS frequency bands. However, the detected intensities are orders of magnitude above the level that each individual satellite would be allowed to have in order to comply with the Rec. ITU-R RA.769-2 thresholds (if all satellites were equally bright as explained in Sect. 3). Therefore, we are of the opinion that satellite operators and regulation authorities should consider satellite UEMR and reflected signals as another aspect of the regulatory process.

Additionally, a dialogue between the satellite operators and the (radio) astronomical community would be welcome to understand how the electrical properties and operational procedures of the satellites affect radio astronomy, and how these can be used

---

[20] Similar figures apply for the broad-band signals. While these have lower intensity, they span many MHz and already the fraction in the RAS band (150.05−153 MHz) leads to the same received power as the higher-intensity narrow-band signal.

to mitigate their impact. Hopefully, this dialogue can build on the co-operation that SpaceX/Starlink has with optical astronomy (see discussion in Green et al. 2022), especially since radio observations may be affected continuously, not primarily during twilight as is the case with optical/infrared astronomy. This could follow the example that was set with the recent coordination agreement between the US National Science Foundation (NSF) and SpaceX. Most of the authors of this work are active members in the IAU CPS, where this dialogue can take place.

It cannot be overstated, that any loss of observing time can directly be translated into a monetary loss of the substantial investments which went into developing, operating and using radio astronomy facilities (e.g. Barentine et al. 2023). However, the much graver consequence is the loss of the output of this comparably small investment – fundamental research is a significant sector of physical science, which usually pays out only in a matter of decades. While some of the existing satellite constellations have the means to protect radio astronomy sites from intended radio transmissions by steering their radio beams away, this kind of active mitigation will not be possible for UEMR. Hence, this is an issue in need of close attention by satellite operators, regulators and the astronomical community. Tens of thousands of low-Earth orbit satellites are in the making and without proper consideration, these could potentially produce an artificial sphere of 'radio light' that leaks into astronomical observations, rendering some astronomical observations impossible.

References

Astropy Collaboration (Robitaille, T. P., et al.) 2013, A&A, 558, A33
Astropy Collaboration (Price-Whelan, A. M., et al.) 2022, ApJ, 935, 167
Barentine, J. C., Venkatesan, A., Heim, J., et al. 2023, Nat. Astron., 7, 252
Bassa, C. G., Hainaut, O. R., & Galadí-Enríquez, D. 2022, A&A, 657, A75
Behnel, S., Bradshaw, R., Citro, C., et al. 2011, Comput. Sci. Eng., 13, 31
Blondeaux, H., Terral, M., Gutierrez-Galvan, R., & Baud, C. 2016, in 2016 ESA Workshop on Aerospace EMC (Aerospace EMC), 1
Boley, A. C., & Byers, M. 2021, Sci. Rep., 11, 10642
Broekema, P. C., Mol, J. J. D., Nijboer, R., et al. 2018, Astron. Comput., 23, 180

Cohen, R. J. 2004, in Spectrum Management for Radio Astronomy, eds. B. M. Lewis, & D. T. Emerson, 146
Committee on Radio Astronomy Frequencies 2005, CRAF Handbook for Radio Astronomy (ESF-CRAF)
Dewey, R. J., Taylor, J. H., Weisberg, J. M., & Stokes, G. H. 1985, ApJ, 294, L25
Di Vruno, F., & Tornatore, V. 2023, in International VLBI Service for Geodesy and Astrometry 2022 General Meeting Proceedings, eds. K. L. Armstrong, D. Behrend, & K. D. Baver, 19
ECC 2011, Impact of unwanted emissions of Iridium satellites on radioastronomy operations in the band 1610.6–1613.8 MHz, Technical report ECC Report 171, Electronic Communications Committee, Tallinn
ECC 2016, Description of the software tool for processing of measurements data of IRIDIUM satellites at the Leeheim station, Technical report ECC Report 247, Electronic Communications Committee, Copenhagen
ECC 2021, Compatibility and sharing studies related to NGSO satellite systems operating in the FSS bands 10.7−12.75 GHz (space-to-Earth) and 14−14.5 GHz (Earth-to-space), Technical report ECC Report 271, Electronic Communications Committee, Copenhagen
Elkman, W. R., Tettemer, G. L., & Hungate, S. R. 2007, in 2007 IEEE International Symposium on Electromagnetic Compatibility, 1
Fleet, R. 2015, in International Meteor Conference Mistelbach, Austria, 30
Green, R. F., Luginbuhl, C. B., Wainscoat, R. J., & Duriscoe, D. 2022, A&ARv, 30, 1
Hainaut, O. R., & Williams, A. P. 2020, A&A, 636, A121
Hobbs, G., Manchester, R. N., Dunning, A., et al. 2020, PASA, 37, e012
Hunter, J. 2007, Comput. Sci. Eng., 9, 90
ITU-R 2003a, Protection criteria used for radio astronomical Measurements, Recommendation RA.769-2, International Telecommunication Union, Geneva
ITU-R 2003b, Reference radio astronomy antenna pattern to be used for compatibility analyses between non-GSO systems and radio astronomy service stations based on the epfd concept, Recommendation RA.1631-0, International Telecommunication Union, Geneva
ITU-R 2007a, Calculation of unwanted emission levels produced by a non-geostationary fixed-satellite service system at radio astronomy sites, Recommendation S.1586-1, International Telecommunication Union, Geneva
ITU-R 2007b, Interference calculations between non-geostationary mobile-satellite service or radionavigation-satellite service systems and radio astronomy telescope sites, Recommendation M.1583-1, International Telecommunication Union, Geneva
ITU-R 2015, Levels of data loss to radio astronomy observations and percentage-of-time criteria resulting from degradation by interference for frequency bands allocated to the radio astronomy service on a primary basis, Recommendation RA.1513-2, International Telecommunication Union, Geneva
ITU-R 2020, Radio Regulations (Geneva: WRC-19/Sharm el-Sheik)
ITU-R 2021a, Characteristics of radio quiet zones, Report RA.2259-1, International Telecommunication Union, Geneva
ITU-R 2021b, Prediction procedure for the evaluation of interference between stations on the surface of the Earth at frequencies above about 0.1 GHz, Recommendation P.452-17, International Telecommunication Union, Geneva
ITU-R Working Party 7D 2013, Handbook on Radio Astronomy (ITU-R)
Johnston, S., Bailes, M., Bartel, N., et al. 2007, PASA, 24, 174
Jones, E., Oliphant, T., Peterson, P., et al. 2001, SciPy: Open source scientific tools for Python
Jonas, J., & MeerKAT Team 2016, in MeerKAT Science: On the Pathway to the SKA, 1
Jouade, A., & Barka, A. 2019, IEEE Access, PP, 1
Kondratiev, V. I., Verbiest, J. P. W., Hessels, J. W. T., et al. 2016, A&A, 585, A128
Lawler, S. M., Boley, A. C., & Rein, H. 2022, AJ, 163, 21
McDowell, J. C. 2020, ApJ, 892, L36
Michal, T., Eglizeaud, J. P., & Bouchard, J. 2005, in ESA Special Publication, 587, 4th European Conference on Space Debris, ed. D. Danesy, 61
National Academies of Sciences, Engineering, and Medicine. 2015, Handbook of Frequency Allocations and Spectrum Protection for Scientific Uses, 2nd Edn. (Washington, DC: The National Academies Press)
Offringa, A. R., van de Gronde, J. J., & Roerdink, J. B. T. M. 2012, A&A, 539, A95
Offringa, A. R., de Bruyn, A. G., Zaroubi, S., et al. 2013, A&A, 549, A11
Petroff, E., Keane, E. F., Barr, E. D., et al. 2015, MNRAS, 451, 3933
Prabu, S., Hancock, P. J., Zhang, X., & Tingay, S. J. 2020, PASA, 37, e010
Pulkkinen, J. P. 2019, in 2019 International Symposium on Electromagnetic Compatibility – EMC EUROPE, 410
Rawls, M. L., Thiemann, H. B., Chemin, V., et al. 2020, RNAAS, 4, 189

Swart, G. P., Dewdney, P. E., & Cremonini, A. 2022, J. Astron. Telescopes Instrum. Syst., 8, 011021

Torne, P. 2017, PhD thesis, Max-Planck-Institute for Radioastronomy, Bonn, Germany

Vallado, D. A., Crawford, P., Hujsak, R., & Kelso, T. 2006, in AIAA/AAS Astrodynamics Specialist Conference, Keystone, CO

van der Walt, S., Colbert, S., & Varoquaux, G. 2011, Comput. Sci. Eng., 13, 22

van Haarlem, M. P., Wise, M. W., Gunst, A. W., et al. 2013, A&A, 556, A2

Walker, C., Di Pippo, S., Aubé, M., et al. 2020a, Dark & Quiet Skies I (2020), Report of the conference held 5–9 October, 2020

Walker, C., Hall, J., Allen, L., et al. 2020b, in Bulletin of the American Astronomical Society, 52, 0206

Walker, C., Di Pippo, S., Aubé, M., et al. 2021, Dark & Quiet Skies II (2021), Report of the conference held 3–7 October, 2021

Winkel, B. 2023, Astrophysics Source Code Library, [record ascl:2303.001]

Winkel, B., & Jessner, A. 2018a, Astrophysics Source Code Library, [record ascl:1810.008]

Winkel, B., & Jessner, A. 2018b, Adv. Radio Sci., 16, 177

Winkel, B., & Jessner, A. 2019, J. Astron. Instrum., 8, 1940002

Winkel, B., Kraus, A., & Bach, U. 2012, A&A, 540, A140

Yavaş, G., & Akgül, S. 2019, in 2019 9th International Conference on Recent Advances in Space Technologies (RAST), 851

Appendix A: The Equivalent-Power Flux Density method (EPFD)

Mathematically, the received aggregated power for a RAS pointing direction, (φ_0, ϑ_0), is given by

$$P_{\rm rx}(\varphi_0, \vartheta_0) = \sum_{i=0}^{n} L_i^{-1}(\varphi_i, \vartheta_i, d_i) G_{\rm rx}(\varphi_i, \vartheta_i; \varphi_0, \vartheta_0) G_{\rm tx}(\tilde{\varphi}_i, \tilde{\vartheta}_i) P_{\rm tx} .$$

(A.1)

The angles (φ_i, ϑ_i) describe the position of satellite i in the observer frame (e.g. azimuth and elevation), while $(\tilde{\varphi}_i, \tilde{\vartheta}_i)$ is the position of the observer in the satellite antenna frame. The distance between each of the satellites and the observer is denoted as d_i. Furthermore, $P_{\rm tx}$ is the transmitted power in forward direction, $G_{\rm tx,rx}$ are the effective transmitter and receiver antenna gains. The path attenuation/path propagation loss is subsumed into $L_i(\varphi_i, \vartheta_i, d_i)$.[21] If only line-of-sight loss would be accounted for (which is approximately correct at low frequencies), L_i becomes

$$L_i^{-1}(d_i) = \left[\frac{1}{4\pi} \frac{c}{d_i f} \right]^2 .$$

(A.2)

where c is the speed of light and f is the observing frequency. At higher frequencies, atmospheric attenuation plays an important role, too.

The received aggregated power as given in Eq. A.1 is not the quantity, which is used in Rec. ITU-R S.1586-1; Rec. ITU-R M.1583-1. Instead, in these recommendations the EPFD is defined as

$$\text{EPFD}(\varphi_0, \vartheta_0) = \sum_{i=0}^{n} \frac{1}{4\pi d_i^2} \frac{G_{\rm rx}(\varphi_i, \vartheta_i; \varphi_0, \vartheta_0)}{G_{\rm rx}^{\max}} G_{\rm tx}(\tilde{\varphi}_i, \tilde{\vartheta}_i) P_{\rm tx} .$$

(A.3)

This assumes pure line-of-sight propagation losses. In this case, we can also identify

$$\text{EPFD}(\varphi_0, \vartheta_0) = 4\pi \frac{f^2}{c^2} \frac{1}{G_{\rm rx}^{\max}} P_{\rm rx}(\varphi_0, \vartheta_0) ,$$

(A.4)

but as mentioned above, it is usually desired to normalise this to a hypothetical isotropic receiver, to make the comparison with Rec. ITU-R RA.769-2 easier, that is

$$\text{EPFD}(\varphi_0, \vartheta_0)|_{G_{\rm rx}^{\max}=1} = 4\pi \frac{f^2}{c^2} P_{\rm rx}(\varphi_0, \vartheta_0) .$$

(A.5)

It should be noted that Rec. ITU-R RA.769-2 also contains limits for the received power, such that it would equally well be possible to directly work with Eq. A.1. In the following, all PFD values are to be understood in the sense of Eq. A.5. The simulations, carried out in this work, perform EPFD calculations for a grid of sky cells as proposed in Rec. ITU-R S.1586-1 and Rec. ITU-R M.1583-1. The applied scheme returns cells that have approximately the same solid angles. Rec. ITU-R S.1586-1 also recommends to use a random pointing of the radio telescope antenna in a given cell for each iteration, but if the grid cells are not too large the final results usually do not show significant

dependence on this. Nevertheless, as this has no impact on the computational complexity, it is usually done in this way.

Radio telescope antenna patterns are very complicated depending on the fine details of the aperture. For example, primary foci are often attached to support legs, which block part of the aperture (as the primary focus installation itself). For general purpose calculations, Rec. ITU-R RA.1631-0 contains a (radially symmetric) reference antenna pattern to be used in spectrum management compatibility studies, which is based on a non-blocked circular aperture.

In the EPFD calculation the transmitter gain as well as the receiver gain have to be accounted for, both being direction dependent. While the receiver gain depends only on the angular separation between a given telescope pointing and a satellite (owing to the symmetry of the Rec. ITU-R RA.1631-0 pattern), the satellite transmitter antenna pattern can be a more complicated function. Therefore, for each time step (and thus satellite position), the relative position of the RAS station in the dynamic satellite antenna frame must be inferred.

---

[21] It is common to define the path propagation loss as a quantity larger than One, such that it is positive on the Decibel scale, which is why one has to divide by L_i in Eq. A.1.